High Strain Rate Deformation Behavior of Dual Phase Steels: The Role of Martensite Volume Fraction and Distribution

A Dissertation Submitted

in partial fulfillment of the requirements
for the degree of

Master of Engineering

in

Production Engineering

by

Manpreet Singh

Registration No.: 801585018

Under the Supervision of

Dr. Tarun Nanda
Associate Professor, MED,
Thapar University, Patiala

Dr. B. Ravi Kumar
Senior Principal Scientist, MTE
CSIR-NML, Jamshedpur

MECHANICAL ENGINEERING DEPARTMENT

THAPAR UNIVERSITY, PATIALA

July, 2017

Dedicated To My Grandfather

Sh. Gurdev Singh

CERTIFICATE

I hereby declare that the thesis entitled **"High strain rate deformation behavior of dual phase steels: the role of martensite volume fraction and distribution"** is an authentic record of my work carried out as requirements for the award of the degree of **Master of Engineering** in **Production Engineering** at **Thapar University, Patiala** under the supervision of **Dr. Tarun Nanda**, Associate Professor, Mechanical Engineering Department, Thapar university, Patiala and **Dr. B. Ravi Kumar**, Senior Principal Scientist, MTE Division, CSIR-NML, Jamshedpur during July, 2015 to July, 2017. No part of the matter embodied in this report has been submitted to any other university or institute for the award of any degree.

Manpreet Singh

Date: 17-07-2017 Manpreet Singh

It is certified that the above statement made by the student is correct to the best of our knowledge and belief.

Dr. Tarun Nanda
Associate Professor
Mechanical Engineering Department
Thapar University, Patiala - 147004

Dr. B. Ravi Kumar
Senior Principal Scientist
MTE Division
CSIR-NML, Jamshedpur -831007

Acknowledgement

Though this dissertation work belongs to me, but there are many people who effortlessly worked with me to complete this work. I would like to thank all those people who made this thesis possible and an unforgettable experience for me.

First of all, I would like to express my deepest sense of gratitude to my supervisor Dr. Tarun Nanda, who offered his continuous advice and encouragement throughout the course of this thesis. I thank him for the systematic guidance and great effort he put into training me in the scientific field.

I would like to express my very sincere gratitude to my second supervisor, Dr. B. Ravi Kumar, for his excellent guidance, caring attitude, patience, and providing me with an excellent atmosphere for doing research. His patience and support helped me to overcome many crisis situations and finish this dissertation.

A special thanks to Mr. Anindya Das, who helped me in the experimentation work on high strain rate testing machine. I am also indebted to the members of the National Metallurgical Laboratory, Jamshedpur with whom I have interacted during my research work. I would also like to thank Mr. Lalan Patro who helped me in my work whenever I needed.

I want to thank my friends, Gurpreet Singh, Nand Kumar Patel, Munish Kunj Pandey, Bhupinder Singh, Jagjit Singh, and Harsh Kansal who created a friendly environment around me and kept me motivated and helped me in my research work also.

Finally and importantly, I take this opportunity to express the profound gratitude from my deep heart to my beloved parents and my brother for providing me with unfailing support and continuous encouragement throughout my years of study and through the process of researching and writing this thesis. This accomplishment would not have been possible without them.

Manpreet Singh

Manpreet Singh

Abstract

Ferrite-martensite dual phase steels (DP steels) are drawing a great demand in the automobile industries for their high strength to weight ratio, excellent formability, and high yield strength to ultimate strength ratio. The presence of hard martensite phase within softer ferrite matrix makes these steels a potential material for microstructural engineering to produce steels with fabulous properties. Moreover, being a potential material in automobile components, dual phase steels are studied extensively in order to evaluate and understand their properties under various loading conditions. The properties of dual phase steels are found to be influenced largely by (a) amount, (b) size and distribution, and (c) morphology of the individual phases. As dual phase steels are extensively used in crash sensitive components, it becomes important to investigate the effect of these microstructural parameters on the deformation behavior of dual phase steels under high strain rate conditions.

In the present work, three different annealing routes viz. CAL, CHCL, and CAS cycle were employed to obtain DP microstructure having different martensite volume fraction, morphology, and distribution. CAL cycle was used to simulate the conventional cycle used in industry to obtain the DP590 grade (referred here as DP-1) having martensite phase distributed on the grain boundaries of ferrite (with martensite fraction ~ 20 %). CHCL cycle was used to obtain in-grain martensite distribution in addition to grain boundary martensite with volume fraction of martensite similar to CAL cycle (DP steel obtained was referred as DP-2). CAS cycle was employed to obtain DP microstructure (referred here as DP-3) having higher volume fraction of martensite (~ 67 %) surrounded by ferrite network/channel distribution. The main focus of present research was to analyze the effect of these different DP microstructures on the tensile properties at different strain rates. The tensile tests were done at different strain rates in the range 2.7×10^{-4} to 650 s^{-1}. In case of DP-1 and DP-2 steels, the UTS and YS increased with increase in strain rate whereas percentage uniform elongation was decreased with increase in strain rate. However, the percentage elongation values of CHCL samples were higher with comparable strength compared to CAL samples for all high strain rate levels. DP-3 showed excellent results at high strain rate conditions. The energy absorption intensity of CAS cycle was highest among the three cycles at high strain rates, CHCL cycle also showed higher energy absorption intensity than the conventional CAL cycle at high strain rate conditions. Modified C-J method was used to analyze the strain hardening behaviour of the three different steels at quasi-static conditions. All the three steels showed three stages of strain hardening. Initial strain hardening rate of the DP-3 was highest

and DP-2 also showed higher initial strain hardening than DP-1 at all strain rate levels. The initial strain hardening rate was increased significantly at higher strain rates for all the three steels. Furthermore, the fracture surface and fracture tips of samples were also characterized in FEG-SEM, to correlate the obtained mechanical properties with deformation mechanisms present in the different DP microstructures used in this study. The higher volume fraction of martensite and core/shell microstructure of DP-3 and in-grain distribution of DP-2 was considered responsible for the improved properties at high strain rates.

Keywords: Dual phase steels; High strain rate; strain hardening rate; Strain rate sensitivity; Energy absorption intensity; Martensite.

Table of Contents

List of Figures

List of Tables

List of Acronyms

Acronym	Full name
AHSS	Advanced high strength steels
DP	Dual phase
YS	Yield strength
UTS	Ultimate tensile strength
TRIP	Transformation induced plasticity
TWIP	Twinning induced plasticity
CP	Complex phase
Q-P	Quenching and partitioning
DARA	Dislocation absorption by retained austenite
HSLA	High strength low alloy
MVF	Martensite volume fraction
IHT	Intercritical holding temperature
SHTB	Split Hopkinson tensile bar
PS	Pre-straining
BH	Bake hardening
SEM	Scanning electron microscope
TEM	Transmission electron microscope
HDPS	Hot dip process simulator
CAL	Continuous annealing line
CHCL	Continuous heating and cooling line
CAS	Core and shell
GNDs	Geometrically necessary dislocations

List of Symbols

Symbol	Meaning
$\dot{\varepsilon}$	Strain rate
℃	Degree Celsius
A_{c1}	Lower critical temperature
A_{c3}	Upper critical temperature
C	Carbon
Mn	Manganese
P	Phosphorous
S	Sulphur
Si	Silicon
B	Boron
Cr	Chromium
Mo	Molybdenum
Ni	Nickel
Fe	Iron
V	Vanadium
Ti	Titanium
Nb	Niobium
Al	Aluminium
Cu	Copper
$R_{p0.02}$	Yield strength
R_m	Ultimate tensile strength
σ	True stress
m	Strain hardening exponent
ε_0	Initial true strain
k	Material constant
ε	True strain
m	Strain rate sensitivity
ΔE	Energy absorption intensity
H_2	Hydrogen
N_2	Nitrogen
m_{QD}	Strain rate sensitivity when shifting from quasi-static to dynamic region
m_D	Strain rate sensitivity in dynamic region.
DP-1	Steel processed by CAL cycle

DP-2	Steel processed by CHCL cycle
DP-3	Steel processed by CAS cycle

Chapter 1
Introduction

1 Introduction

1.1 General

This chapter discusses briefly about advanced high strength steels (AHSS) and their properties. The classification of AHSS based on microstructure and properties, the deformation mechanisms, microstructure, properties and applications of different grades of AHSS is also discussed. This chapter explains about strain rate and need for testing at high strain rate. Furthermore, this chapter elaborates on the microstructure, processing, mechanical properties, applications and properties at high strain rates of dual phase (DP) steels.

1.2 Advanced high strength steels (AHSS)

Vehicle safety during crash and light weight of body to reduce fuel consumption have become important considerations for automobile industry. A light weight body with enhanced vehicle safety requires materials which have high specific strength and can dissipate maximum energy during the crash. Advanced high strength steels (AHSS) are a newly developed category, which have expanded applications in automobile industry. AHSS provide good combinations of strength and formability as compared to conventional high strength steels [1–3].

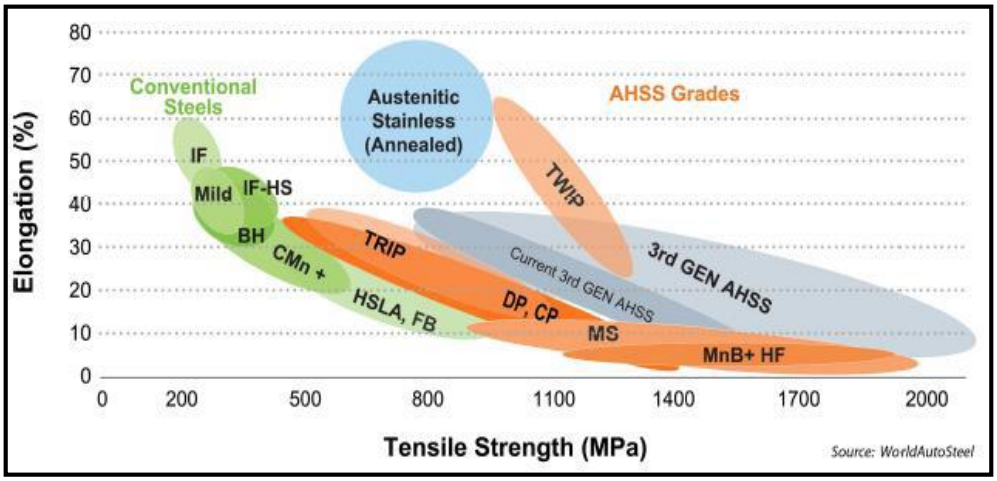

Figure 1.1: Strength and percentage elongation of various types of steels [4].

The strength and percentage elongation of various steels are shown in Fig. 1.1. From Fig. 1.1, it is clear that AHSS provide better combination of strength and percent elongation [4].

Table 2.1: Microstructure, industrial applications, properties and deformation mechanisms of different AHSS.

Type of AHSS	Room temperature microstructure	Deformation mechanism and properties	Grades of AHSS and their automotive applications
TRIP	Ferrite (50–55%) + Bainite (30–35%) + Retained austenite (7–15%) + Martensite (1–5%)	*Deformation Mechanism:* TRIP effect: retained austenite converts to martensite during deformation. *Properties:* Superior combination of strength and ductility. *Limitations:* Poor local and edge stretchability, poor cost effectiveness	TRIP 350/600 is used in rail reinforcements
			TRIP 400/700 is used in crash box and side rail
			TRIP 450/800 is used in roof rails and dash panel
			TRIP 750/980 is used in seat frame, engine cradle, front and rear rails
TWIP	Austenite	*Deformation Mechanism:* Dislocation glide and mechanical twinning. *Properties:* Excellent strength-formability combination. Formability is more than TRIP, DP, CP steels. *Limitations:* Low productivity in processing, high alloy addition reduces cost effectiveness, and fracture delay.	TWIP 500/900 is used in A-Pillar
			TWIP 500/980 is used in front and rear bumper beams and B-pillar
			TWIP 600/900 is used in wheel-house and floor cross-member
			TWIP 950/1200 is used in door impact beam
DP	Ferrite matrix + second phase as martensite or bainite	*Deformation Mechanism:* Dislocation glide. *Properties:* High specific strength, continuous yielding behaviour, good initial work hardening, and high bake-hardenability. *Limitations:* Limited formability.	DP 300/500 is used in floor panel, door outer, roof outer, body side outer
			DP 350/600 is used in floor reinforcements, cowl, fender
			DP 500/800 is used in rear shock reinforcements, quarter panel inner
			DP 600/980 is used in front sub-frame package tray, safety cage components, floor panel tunnel, engine cradle
			DP 700/1000 is used in roof rails
CP	Fine ferrite/bainite matrix + small volume fraction of martensite and pearlite	*Deformation Mechanism:* Dislocation glide (occurs mainly in ferrite-bainite matrix) *Properties:* High ultimate tensile strength of more than 800 MPa. Continuous yielding and high uniform elongation *Limitations:* Decreased formability at high strength values	CP 680/780 is used in transverse beams, chassis components
			CP 750/900 is used in tunnel stiffener and B-pillar reinforcements
			CP 800/1000 is used in fender beam, rear suspension brackets
			CP1050/1470 is used in bumper beams and rocker panels
Q-P	Ferrite + martensite + retained austenite.	*Deformation Mechanism:* TRIP effect and DARA(dislocation absorption by retained austenite) effect *Properties:* Best combination of strength and ductility *Limitations:* For DARA effect, at-least 10% RA (retained austenite) required in the microstructure	Currently under development. Yet not in industrial use.

AHSS are defined as steels which possess yield strength (YS) greater than 300 MPa and ultimate tensile strength (UTS) equal to or greater than 550 MPa. The superior strength-formability combination in AHSS is derived from complex/ multiphase microstructures (containing martensite, ferrite, bainite, and/or retained austenite) [4–8]. Industrial

applications, properties and deformation mechanisms for different AHSS are presented in Table 1.1.

1.2.1 Classification of AHSS

AHSS steels are mainly classified as first generation, second generation, and third generation AHSS.

1) **First generation AHSS**: AHSS of first generation have ferrite as the main phase and mainly include DP steels (dual-phase), CP steels (complex-phase), TRIP steels (transformation-induced plasticity). The strength level of first generation AHSS is higher than conventional micro-alloyed (HSLA) steels, but insufficient formability still remains a major problem [5–9].
2) **Second generation AHSS**: In order to overcome the problem of insufficient formability in the first category of AHSS, the second generation steels were developed which show excellent combination of strength and formability. Second generation AHSS include L-IP steels (Light-weight with induced plasticity), TWIP steels (Twinning induced plasticity), and SIP steels (Shear band formation-induced plasticity). These steels have better mechanical properties due to austenitic microstructure. To stabilize austenite in the microstructure at room temperature, second generation steels contain high alloying content (i.e. Mn, Ni etc.) which results in very high cost [8–11]. High cost is a problem with second generation steels which restricts their extensive use [8].
3) **Third generation AHSS**: In order to overcome the limitations of first and second generation AHSSs, the third generation AHSS are being developed, which provide superior strength-formability combination but at lower cost. Third generation is an extension of first generation AHSS by improving their mechanical properties through various techniques like grain refinement, improved processing routes etc [8, 10–13]. DP, TRIP, and CP steels are preferred for being modified and developed into third generation of AHSS [8, 10, 11, and 14].

1.3 Strain rate

Strain rate ($\dot{\varepsilon}$) is defined as the rate of change of strain (ε) with respect to time (t).

$$\dot{\varepsilon} = \frac{d\varepsilon}{dt} \quad \text{..... (1.1)}$$

Where, ε can be either the engineering or the true strain. The unit of strain rate is s^{-1}.

1.3.1 Classification of strain rate

There are three main types of strain rates discussed in literature [15] viz. low, intermediate, and high strain rates.

1) **Low strain rate:** The range of strain rate from 10^{-6}–10^{-3} s^{-1} is considered as quasi-static region and is known as low strain rate.
2) **Intermediate strain rate:** The range of strain rate from 10^{-3}–10^{2} s^{-1} is generally referred to as the intermediate or medium strain-rate condition.
3) **High strain rate:** Strain rates of 10^{2} s^{-1} or higher are generally referred to as high strain-rate response.

1.4 Need for testing at high strain rate

In order to produce vehicles with higher fuel efficiency for satisfying gas-emission regulations and with safety even during severe accidents, the crash analysis of vehicles is very important. In an automobile crash, the deformation occurs at strain rates ranging from 10^{2} –10^{3} s^{-1}. So, in order to carefully and accurately analyze deformation during a crash, the accurate material deformation data at high strain rates (10^{2}–10^{3} s^{-1}) is required [16–18]. The mechanical properties and deformation behavior of steels is different under different strain rate conditions. It has been observed by various researchers that yield strength and tensile strength increase with increase of strain rate. However with the increase in temperature, the strength decreases. Therefore, it is important to analyze the effect of change of strain rates on the mechanical properties of various types of steel [18].

1.5 Dual phase steels

Dual phase (DP) steels are the most commonly used AHSS grade in the automobile sector, especially in the car industry. DP steels contain two phases in their microstructure, a ferrite matrix and a hard second phase (bainite or martensite) [19–25]. The mechanical properties of DP steels depend on grain size of ferrite phase, and on the volume fraction, morphology, and distribution of hard phase present in the ferrite matrix [4, 19, 22, 25]. DP steel grades are designated by a number, which presents the ultimate tensile strength of that grade in MPa. For example, DP600 is a DP grade having an ultimate tensile strength of 600 MPa [26]. DP steels with ferrite-bainite dual phase microstructure possess higher ductility and toughness while those with ferrite-martensite microstructure show higher ultimate tensile strength and yield strength [21]. Martensite content in DP steels is generally varied in the range of 20–70 % depending upon requirements of strength [27, 28].The strength of DP steels also increases

to a certain limit by refining the grain size of ferrite phase, but this increased strength is accompanied with a little loss in ductility [19]. Dual phase steels are low-carbon (up to 0.2 wt. %) steels with manganese and silicon in the range of 1–2 wt. % and 0.05–0.6 wt. % respectively. DP steels also contain micro-additions of molybdenum, titanium, vanadium, and nickel [29–31].

1.5.1 Processing of DP steels

Dual phase steels are generally processed by heating a low-carbon micro-alloyed steel to above the upper critical temperature, holding it there for some time, slowly cooling it to an inter-critical temperature for formation of requisite amount of ferrite phase, and then rapidly cooling it to room temperature for transforming available austenite into martensite [32–34]. In another method reported in literature to process DP steels, the steel is heated to an inter-critical temperature to obtain an austenite-ferrite microstructure, is held there for some period of time, and is finally quenched to room temperature to convert the available austenite into martensite [29, 35, 36]. The former method obtains relatively larger grain size and results in lesser strength but improved ductility as compared to the latter method.

1.5.2 Mechanical properties and applications of DP steels

DP steels are extensively used in automobile industry because of their good combination of high strength and ductility, good weldability, and ability to absorb large amount of crash energy [29, 37]. This AHSS grade displays continuous yielding, high work hardening rates, and low ratio for yield strength to ultimate tensile strength [38–41]. DP steels can be processed to show different strength–ductility combinations by changing the volume fraction of constituent phases, distribution of the second hard phase in the ferrite matrix, carbon content in the harder phase, and grain size [42–44].The characteristic properties of DP steels enable the automobile industry to make light weight, fuel efficient, crashworthy, and safe vehicles. DP steel grades are used to create different car components including wheel discs, rims, bumpers, door reinforcements, brake components, steering couplings, doors, fuel tanks, hood outer, and inner panels [45–51]. DP steels are also finding extensive use in farm equipment, and heavy construction units.

1.5.3 Influence of change of strain rate on properties of dual phase steels

The yield strength and ultimate tensile strength of DP steels, in general, are higher for higher strain rates but are lower for higher temperatures. The increased strengths at higher strain rates are achieved at the expense of loss in ductility [1, 2, 28, 40, 41, 52]. Beynon *et al.* [28]

observed that DP500 and DP600 steels used in automotive industry displayed a significant difference in tensile properties under low and high strain rate testing conditions. Cao *et al.* [52] investigated a commercial dual phase steel grade DP800 and observed increase in flow stress with increase in strain rate and decrease in temperature. Uniform elongation decreased with increase in strain rate at room temperature and at -60 ℃, but at 100 ℃ uniform elongation increased with increase in strain rate. Cao *et al.* [40] observed that pre-straining and bake-hardening of DP800 steel increased the strength, decreased strain hardening and ductility at all temperatures and strain rates. Kim et at. [53] investigated the plastic anisotropy in different orientations (RD, TD and DD) for DP780 and TRIP780 steels at high strain rate. The authors observed that plastic anisotropy did not change significantly for both materials, but strength for DP780 steel increased in TD direction. Wang *et al.* [41] studied the strain rate sensitivity of DP600, DP800, DP1000, and martensitic steel (MS 1200) having different martensite volume fractions (MVFs). All DP grades showed positive strain rate sensitivity but the increment in strength decreased with increase in MVF. The MS 1200 steel showed negative strain rate sensitivity.

1.6 Summary of the chapter

The demand for fuel efficient, light weight, and crash-resistant automobiles has increased the use of advanced high strength steels (AHSS) in automobile industry. AHSSs have excellent strength-formability combinations which help in reduction of vehicle weight and improve the efficiency without affecting crashworthiness. These are classified as first generation AHSS, second generation AHSS and third generation AHSS according to their strength and formability combinations. First generation provides good strength, but the insufficient strength is still a problem. Second generation AHSS provide good strength and good formability, but high cost restricts their extensive use. In order to overcome the limitations of first and second generation AHSS, third generation AHSS are being developed, which provide superior strength-formability combination but at lower cost. Dual phase (DP) steels are the most important AHSS grade used in automobiles. DP steels generally consist of ferrite-martensite dual phase microstructure in which the hard phase martensite is present in the soft ferrite matrix. DP steels exhibit continuous yielding, good strength-formability combination, low yield strength to ultimate strength ratio (YS/UTS), and high work hardening rates. Due to these excellent properties, DP steels are used for making various structural components in automobiles. During collision of an automobile, high strain rate up to 500 s^{-1} or more can be encountered. As AHSS are used in automobiles, so their testing at

high strain rates is very important to analyze their mechanical properties during crash conditions.

Chapter 2
Literature Review

2 Literature Review

2.1 General

This chapter presents a detailed literature review on processing and properties of dual phase steels with emphasis on the effect of high strain rates on the mechanical properties of advanced high strength steels. It then presents the summary of literature and brings forth the main gaps in it.

2.2 Review of the existing literature

Conception *et al.* [54] investigated the influence of amount of carbon (present in steel) on microstructure and mechanical properties of dual phase steels. Chemical composition of the investigated materials with different carbon content ranging from 0.08 to 0.38 wt% is shown in Table. 2.1. DP steels with different volume fractions of martensite were obtained by various inter-critical heat treatments of steel samples having different amount of carbon. Microstructural characterization, micro-hardness, and tensile tests were performed for each condition.

Table 2.1: Chemical composition of material (wt. %) and critical temperatures (℃) [54].

Material	C	Mn	Si	P	S	Ac_1	Ac_3
S1	0.08	0.77	0.21	0.017	0.012	732	873
S2	0.11	0.69	0.21	0.025	0.021	733	865
S3	0.20	1.45	0.40	0.015	0.028	720	776
S4	0.38	1.43	0.37	0.024	0.033	736	805

It was found that increase in carbon content decreased the intercritical temperature range in which austenite and ferrite coexist. Increase in intercritical holding temperature (IHT) increased the volume fraction of martensite present in DP microstructure, which was due to the higher austenite fraction formed. Martensite fraction also increased with increase in carbon content for the same IHT temperature. In all cases, the hardness values, yield strength, and tensile strength increased with increase in martensite and with increase of carbon in martensite for same volume fraction. Elongation values showed the opposite trend. The best combination of properties was observed for steel having carbon content in the range 0.1 to 0.15 % and with 50 % of martensite volume fraction.

Sudersanan *et al.* [55] studied the change in strength of dual phase steel with the variation of carbon content in second phase martensite present in DP microstructure. Chemical composition of studied steel is shown in Table 2.2.

Table 2.2: Chemical composition of steel [55].

Element	C	Mn	S	P	Si	Cr	Mo	B	Ni
Weight %	0.13	1.18	0.01	0.001	0.3	0.047	0.057	0.001	0.048

The specimens were heat treated in the temperature range of 730 ℃ to 810 ℃, to obtain different volume fractions of martensite in DP structure. The volume fraction of martensite increased with increase in annealing temperature. Martensite as a hard phase dispersed in soft ferrite matrix provides strength to the dual phase steels, however soft ferrite provides ductility. Strength increased initially with martensite volume fraction and then decreased for higher percent of martensite as shown in Fig. 2.1a.

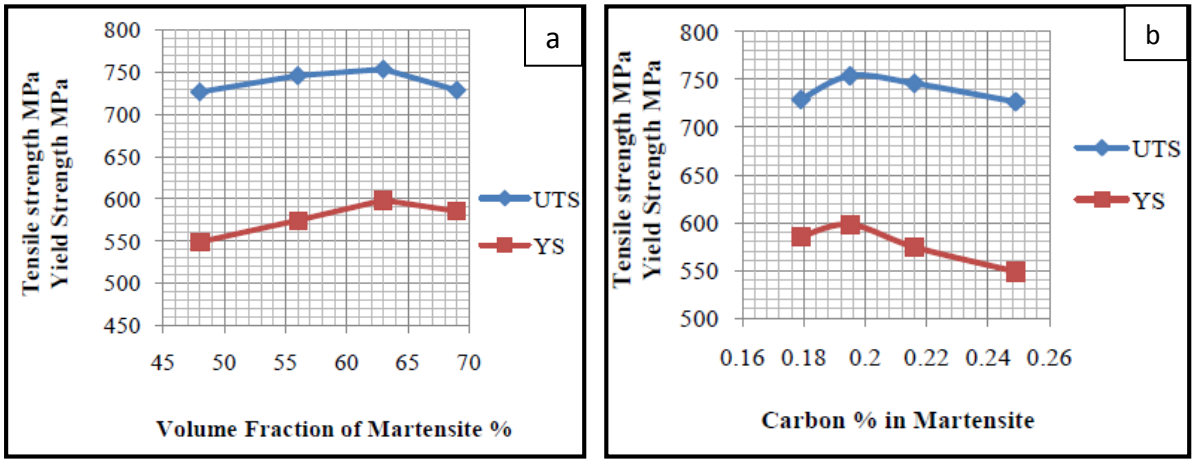

Figure 2.1: (a) Yield and Tensile Strength v/s Volume Fraction of Martensite (b) Yield and Tensile Strength v/s Carbon % in Martensite [55].

The carbon content in the martensite was found to decrease with increase of martensite fraction. Yield strength and ultimate tensile strength increased with increase in carbon content in martensite to a certain limit as shown in Fig. 2.1b. Yield strength and tensile strength was found to increase initially with carbon content up to 0.195 % and then decreased with increase in carbon content in the martensite phase.

Uenshi *et al.* [56] studied the methods for testing of high strain rate properties of sheet materials and made improvements in one bar method to eliminate effect of vibrations in one side of the bar. Further, the authors also studied the effect of high strain rates on the strength of materials. The characteristics of mild steel, 440 MPa steel, DP steel, and TRIP steel were compared at static and dynamic strain rate conditions. To measure high strain rates servo-

hydraulic method, split-Hopkinson method, and one bar method were used as shown in Fig. 2.2.

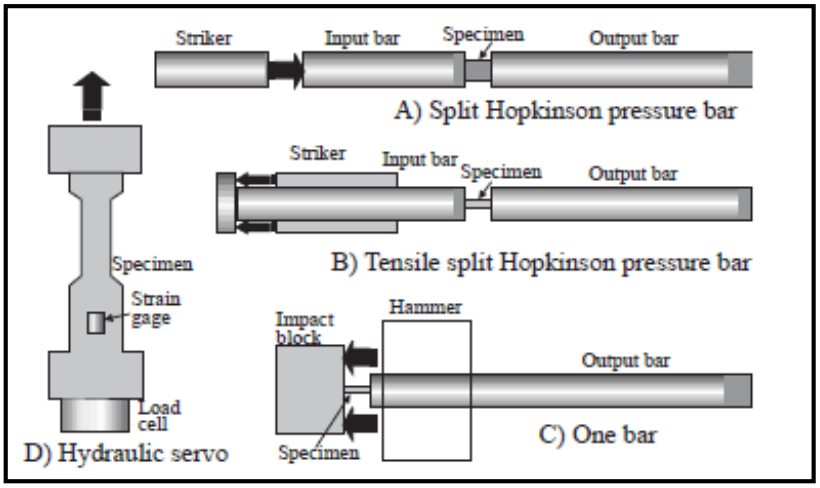

Figure 2.2: Various high strain rate deformation test methods [56].

Servo hydraulic method can measure strain rates from 200 to 300 s^{-1}. Split-Hopkinson method used two bars (input bar and output bar) arranged coaxially. A yoke was attached on input bar and to perform the tensile test this yoke was striked by a striker. By this method, it was difficult to measure stress-strain characteristics until materials ruptured. One bar method used only one bar and test specimen was attached to one end of this bar. Hammer was striked to impact blocker attached to the test specimen to carry out the tensile test. This method enabled the measurement of material behaviour until fracture of material. This method showed a larger stress peak in the initial stage of deformation. To prevent the large stress peak in initial stage, fixing jigs were attached to the output bar end to secure the coaxiality of output bar and impact block.

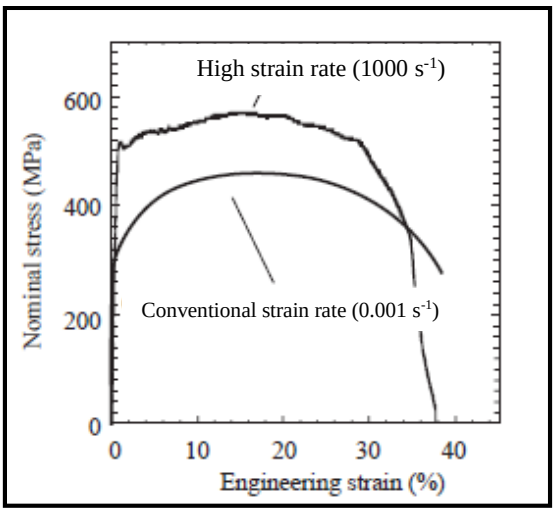

Figure 2.3: Comparison between static and dynamic characteristics [56].

Tensile tests were performed on different steel materials in static and dynamic condition of strain rates by using the above described methods. The results obtained are shown in Fig. 2.3. It was found that for steels with higher static strength, the strain rate sensitivity of flow stress was lesser. But there were some steels like DP and TRIP for which strain rate sensitivity of flow stress was higher than conventional steels, even at 590 MPa static strength.

Gerlach *et al.* [57] developed the design of the split Hopkinson tensile bar (SHTB) and conducted experiments to demonstrate the modified design. The new design used a U-shaped striker bar as projectile instead of the hollow striker bar in old design as shown in Fig. 2.4.

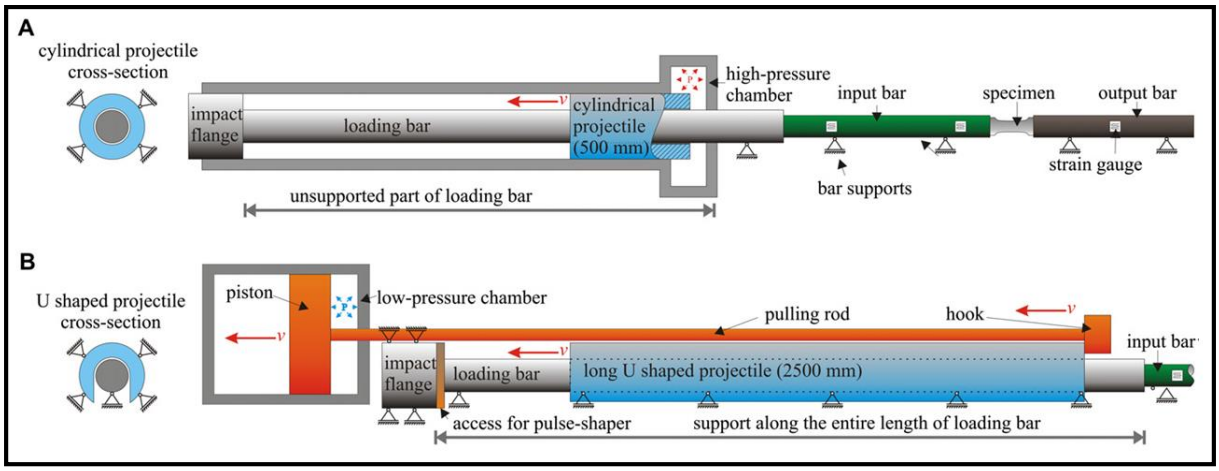

Figure 2.4: (A) Old and (B) new design for the tensile Split Hopkinson Bar apparatus [57].

The new SHTB design was built around a titanium loading bar of 3.6 m length and 20 mm diameter. To generate the input signal, a striker was manufactured from an annealed titanium solid cylindrical bar by machining a slot of 24 mm width along its entire length. The U shaped striker surrounded the loading bar, without having contact with it. The U shaped cross section made provision to support the loading bar along the entire length to prevent it from bending. The 1 ms duration pulse was achieved with the new design, which was 0.2 ms in case of old design as shown in Fig. 2.5. To demonstrate the ability of this new design, experiments were performed on three aluminium alloys and three different steels. The three steel specimens of different steels were tensile tested under various strain rates ranging from 180 s^{-1} to 500 s^{-1} whilst the aluminium alloy specimens were tested at strain rates ranging from 700 s^{-1} to 1500 s^{-1}. The results demonstrated that the developed SHTB design can generate nearly oscillation free stress strain diagrams.

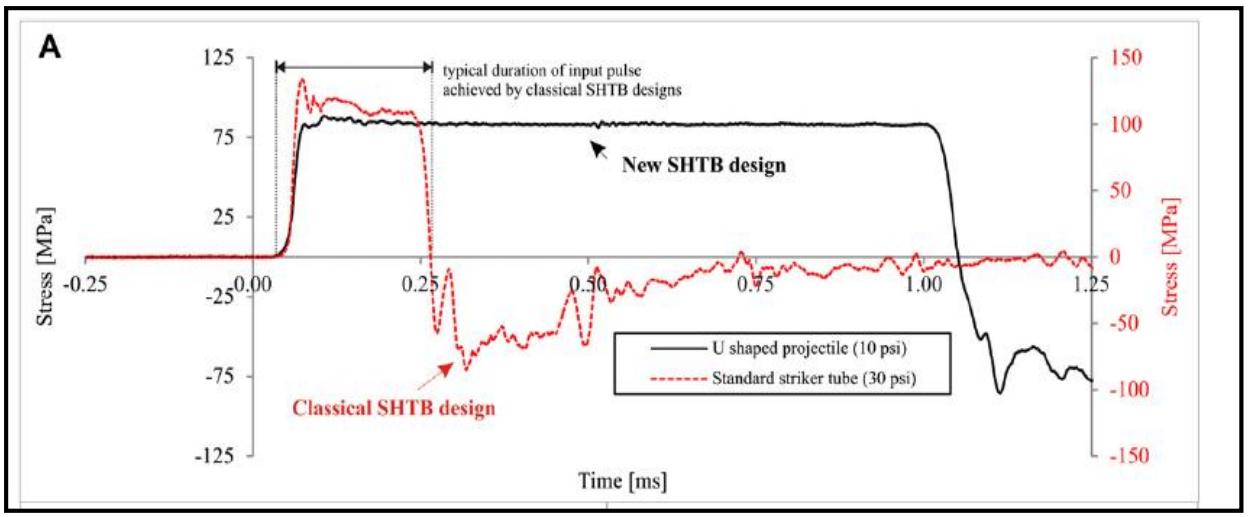

Figure 2.5: Comparison of stress signal duration for new design and old design [57].

Uenishi *et al.* [1] investigated strain rate sensitivity of the flow stress and material strengthening by addition of different solute atoms (Si and Mn) in base material. The base material Fe was alloyed with nominal addition of Si or/and Mn. One bar method was utilized to obtain stress-strain diagrams for strain rates greater than 100 s^{-1}. The material behaviour at large strains was measured by simple shear tests, which was usually difficult to evaluate by tensile tests due to the onset of necking phenomenon.

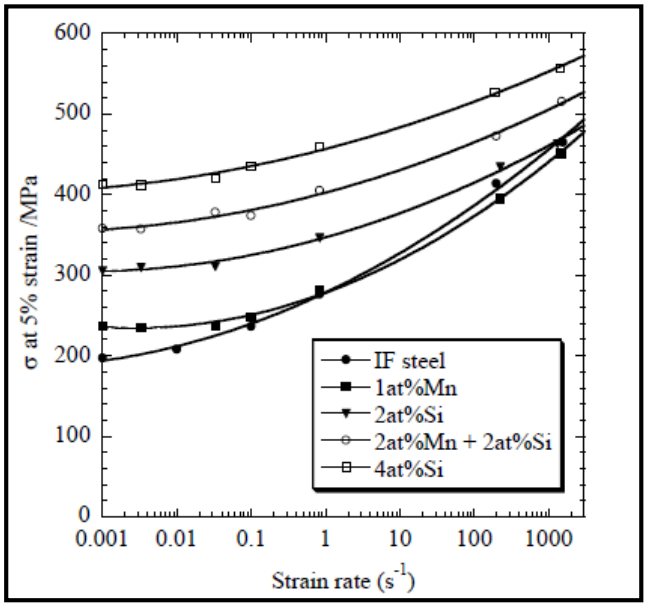

Figure 2.6: Variation of the true tensile flow stress with strain rate at 5 % strain at room temperature [1].

A planner simple shear test machine was used in order to characterize material behaviour at large strain rates. The flow stress was increased with the addition of solute atoms, for low strain rates, whereas at higher strain rates its effect became less pronounced as shown in Fig.

2.6. The strain rate sensitivity of flow stress had a close relation with the hardness of a softer phase present in steel as shown in Fig. 2.7.

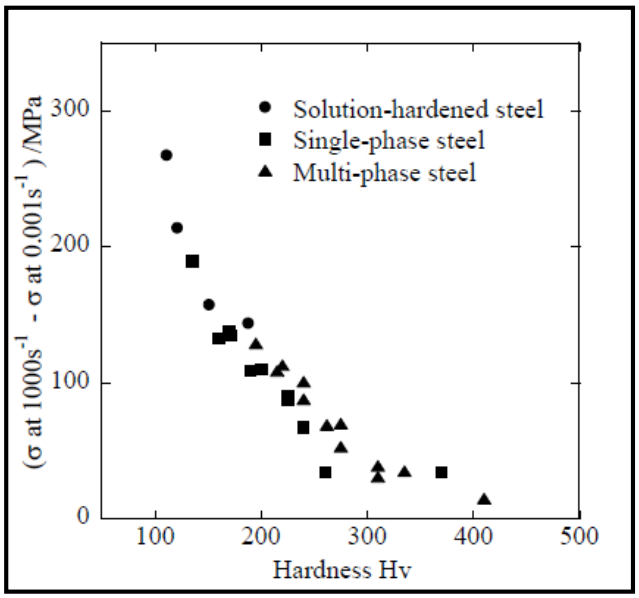

Figure 2.7: Variation of strain rate sensitivity of flow stress with hardness of softer phase [1].

It was found that the strain rate sensitivity of flow stress decreased with quasi static strength and the hardness of the softer phase could be used as an index of strain rate sensitivity of the flow stress in commercial high strength steel sheets. Thus, multi phase steels such as dual phase and TRIP steels had superior strain rate sensitivity of flow stress as compared to that of single phase steels with similar quasi static flow stress, since they contained the softer ferrite as a main phase.

Beynon *et al.* [28] studied the low and high strain rate deformation behaviour and the microstructure of steel sheet components used by automotive industry. The composition of five strip steel grades used was as given below in Table 2.3.

Table 2.3: Composition of steel grades, wt. % [28].

Steel	C	Si	Mn	P	Cr	Mo	Ni	Al	Ti	V	Fe
M/S	0·030	0·006	0·23	0·011	<0·01	<0·001	0·017	0·048	<0·01	<0·001	Bal.
CMn	0·139	0·069	0·78	0·025	<0·01	<0·001	0·014	0·033	<0·01	<0·001	Bal.
DP1	0·092	0·083	1·40	0·017	0·454	0·003	0·021	0·034	0·031	0·002	Bal.
DP2	0·118	0·394	1·41	0·019	0·210	0·052	0·022	0·035	0·010	<0·001	Bal.
DP3	0·106	0·316	0·79	0·010	0·022	0·001	0·039	0·047	<0·01	0·01	Bal.

*M/S is mild steel, CMn is C–Mn steel, DP is dual phase steel.

An electro-servohydraulic universal test machine was used to carry out tests at the slow strain rate of 0.001 s^{-1}, with a load capacity of 100 kN and tests at the strain rate of 100 s^{-1} was conducted on servohydraulic high rate impact machine. Grain size measurements were done

using optical microscope. Microhardness testing was done using a Leco microhardness tester model M–400–G2. The grain elongation and microhardness were measured at different points in the plastic deformation region and were plotted as a function of the distance from the fracture tip of the specimen. Under high strain rate loading conditions, the mild steel with ferritic microstructure did not showed significant change in grain shape. For all steel grades studied, proof stress and tensile strength values was increased with increase in strain rate under dynamic tensile testing conditions, mild steel grade showed considerably higher strain rate sensitivity among all steels. There was a continuous reduction in hardness values when measured from the fracture tip of sample toward undeformed region. In the undeformed region the hardness was remained constant. The DP1 (DP500) and DP2 (DP600) steels showed a noteworthy difference in tensile properties when tested under low strain rate conditions. However, the difference under dynamic strain rate conditions was considerably reduced. This might indicate that the microstructure of the dual phase steel had significant influence under high strain rate conditions than the role of the strengthening additions.

Cadoni *et al.* [58] investigated the strain rate sensitivity of DP1200 and DP1400 under tensile loads at different strain rates in the range of 0.001 s^{-1} to 600 s^{-1}. The composition of these steels was as given below in Table 2.4. Flat steel sheet specimens were tested at room temperature (20 ℃) by using electromechanical universal testing machine to obtain their stress-strain data at strain rate of 0.001 s^{-1}. The mechanical behaviour at medium (3 s^{-1}, and 18 s^{-1}) and high strain rates (200, 400, and 600 s^{-1}) was studied using hydro-neumatic machine and modified Split Hopkinson bar respectively. The tensile tests were also conducted at high temperature (200 ℃) under quasi-static strain rate, the decrease in tensile flow stress was observed with increase in temperature. The stress-strain data was analyzed to determine the material parameters of Cowper-Symonds and the Johnson-Cook models. Results predicted by Johnson-Cook model and Cowper-Symonds model were also compared with experimental true stress versus true strain curves at different strain rates. From the conducted experiments at different strain rates, it was found that:

1. The ratio of yield strength to ultimate tensile strength varied from 0.75 to 0.96 in both the materials. Hence, these materials can dissipate large amount of crash energy.
2. Both the materials exhibited ductile fracture under all strain rate conditions. Ductility of DP1200 was more than DP1400. DP1400 showed greater values of yield stress than DP1200.

Table 2.4: Chemical composition of DP1200 and DP1400 [58].

Constituents (wt.%)	DP1200	DP1400
C	0.120	0.190
Ni	0.040	0.040
Cr	0.030	0.020
Mn	1.600	1.200
Si	0.200	0.200
Mo	0.200	0.200
V	0.010	0.007
Cu	0.005	0.007
Al	0.035	0.040
P	0.010	0.007
S	0.005	0.004
Nb	0.001	0.002
Ti	0.030	0.030
Fe	Balanced	Balanced

3. Both materials exhibited low strain rate sensitivity. The strain rate sensitivity of DP1200 was higher than DP1400.
4. Johnson-Cook model predicted the experimental data to a good extent.

Cao *et al.* [52] investigated the influence of temperature and strain rate on the properties of a industrially used dual phase steel grade DP800. Chemical composition of the steel is shown in Table 2.5. Uniaxial tensile tests were performed on different temperatures (-60 ℃ to 100 ℃) and different strain rates ($1x10^{-4}$ to $1x10^{2}$ s^{-1}).

Table 2.5: Chemical composition of the studied steel (wt%) [52].

C	Si	Mn	P	S	Cr	Ni	Mo	Cu
0.11	0.2	1.4	0.0091	0.0038	0.03	0.05	0.010	0.01
V	**Al**	**Sn**	**Ti**	**As**	**B**	**Nb**	**Co**	**N**
0.0063	0.0424	0.0029	0.0024	0.0016	0.0003	0.014	0.015	0.0086

The influence of temperature and strain rate on the YS and UTS are shown in Fig. 2.8. At all the conditions, the material gave continuous yielding and high strain hardening as revealed by large strain hardening ratios ($R_m/R_{p0.02}$). The flow stress was found to increase with increase in strain rate and opposite trend was obtained with increase in temperature. The uniform elongation decreased with increase in strain rate at room temperature and at -60 ℃, but at 100 ℃ uniform elongation increased with increase in strain rate as shown in Fig. 2.9. The reduction in area increased with increase in strain rate at room temperature. This is an opposite trend to uniform elongation, which is due to the local deformation at high strain rates.

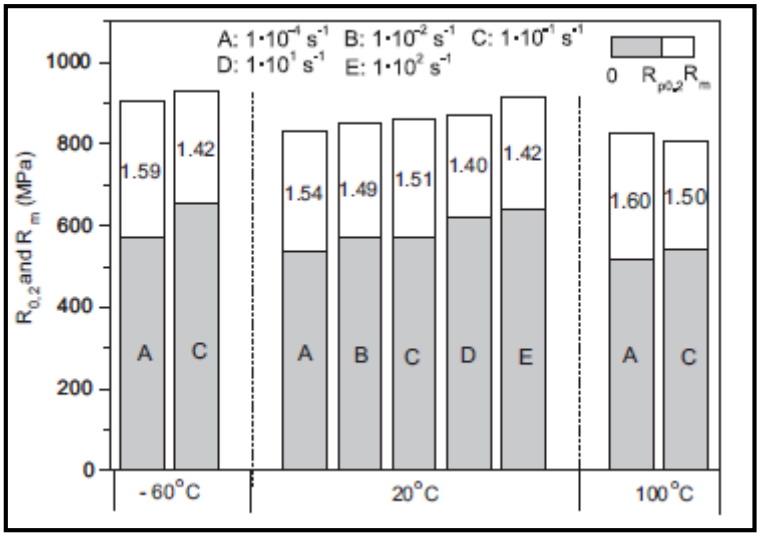

Figure 2.8: Yield and ultimate tensile strengths as a function of strain rate and temperature. Numbers in the columns denote ratios Rm/Rp0.2 [52].

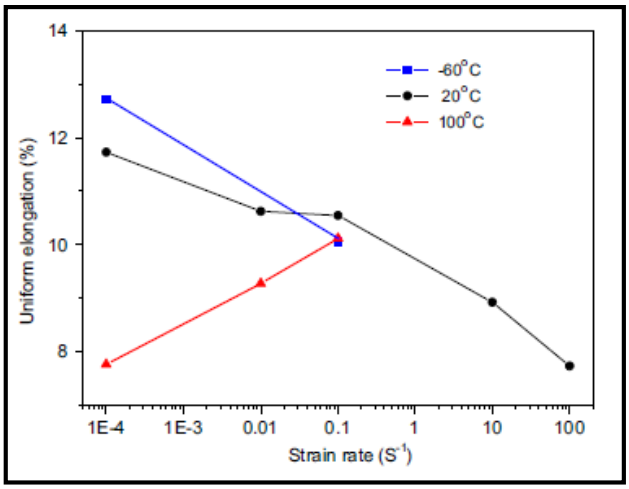

Figure 2.9: Uniform elongation as a function of strain rate and temperature [52].

Cao *et al.* [40] studied the influence of temperature, strain rate, and the paint-bake cycle on the properties of dual phase steel with chemical composition as shown in Table 2.6.

Table 2.6: Chemical composition of as-received steel wt. % [40].

Element	**C**	**Si**	**Mn**	**P**	**S**	**Cr**	**Ni**	**Mo**	**Cu**
Composition	0.111	0.2	1.4	.009	.0038	0.03	0.05	0.01	0.01
Element	**V**	**Al**	**Sn**	**Ti**	**As**	**B**	**Nb**	**Co**	**N**
Composition	0.0063	0.0424	0.0029	0.0024	0.0016	0.0003	0.0136	0.015	0.0086

Dual phase (DP800) steel was strained to 3.5 % followed by annealing at 180 ℃ for 30 minutes to simulate the effect of pressing of sheets and paint-bake cycle during the production of sheet components used in automobile. The influence of temperature and strain rate on the mechanical behavior of materials was investigated as shown in Fig. 2.10.

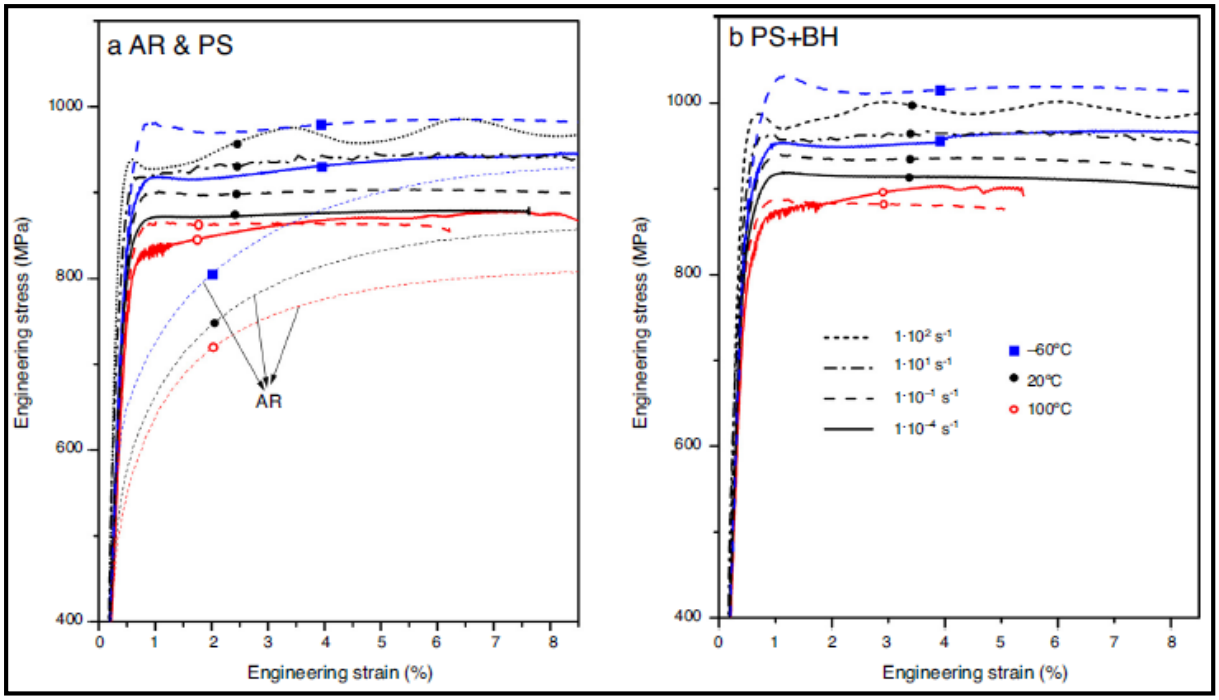

Figure 2.10: Engineering stress–strain relationships for different pre-treatments: (a) as-received (AR) and pre-strained (PS) respectively; (b) pre-strained (PS) + bake hardened (BH) [40].

Pre-straining and bake-hardening led to increase in strength and decrease in strain hardening. Pre-straining and bake-hardening decreased ductility for all temperatures and strain rates used in the present work. Furthermore, pre-straining led to yield point phenomenon through strain aging which was further enhanced by subsequent bake-hardening. Yield strength and ultimate strength were increased with increase in strain rate, and decreased with increase in temperature. For all pre-treatments, there was decrease of uniform elongation with increase in strain rate, however total elongation and reduction in area was increased.

Kim *et al.* [53] studied the influence of high strain rate (0.1 to 500 s^{-1}) on the mechanical properties of DP780, DP980 and TRIP780. Chemical composition is as shown in Table 2.7. For DP780 and TRIP780 steels, tests with different orientations (RD, TD and DD) were conducted to evaluate plastic anisotropy at high strain rate. Anisotropy was not much significant for both materials.

Table 2.7: Chemical composition of the materials (wt. %) [53].

Steel	C	Mn	P	S	Si
DP780	0.070	2.26	0.012	0.003	1.06
TRIP780	0.143	1.99	0.016	0.004	1.31
DP980	0.065	2.40	0.023	0.004	0.076

For both materials, TE increased as shown in Fig. 2.11a. This was due to the effect of strain rate sensitivity on formability. Similar trend was observed for TRIP780 steel (see Figure 2.11b). Both materials showed almost same UTS and the increase of UTS was lower than the increase of YS.

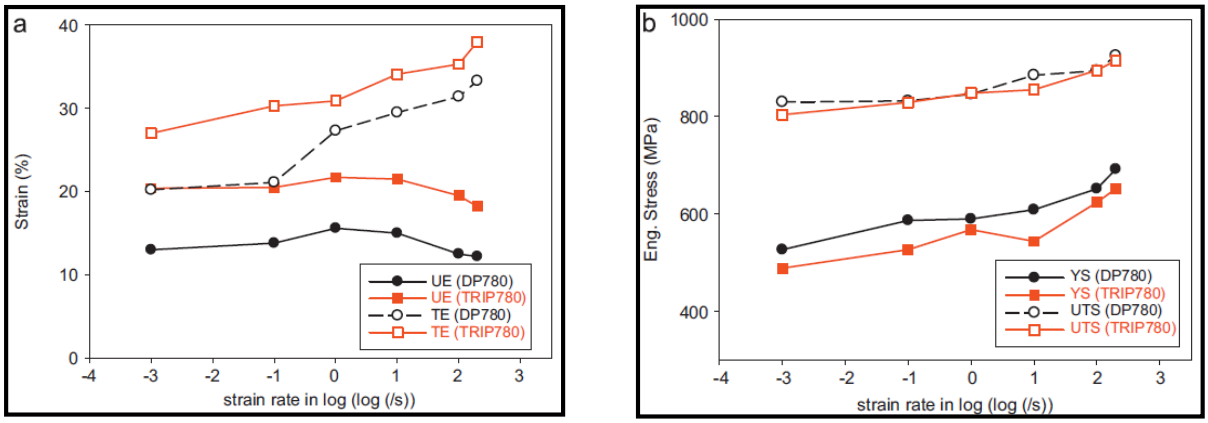

Figure 2.11: (a) Uniform elongation and total elongation in the uniaxial stress–strain curves and (b) yield stress and ultimate tensile strength of DP780 and TRIP780 as a function of strain rate in log-scale [53].

Colla *et al.* [59] investigated the effect of addition of aluminium, boron, and phosphorus on the microstructure and mechanical properties of DP600 and DP450 steels. The Hollomon and Pickering models were also studied to predict the strain hardening behaviour of investigated steels. Chemical composition of different DP steels is shown in Table 2.8.

Table 2.8: Chemical composition of DP steels [59].

Steel	C (Wt Pct)	Mn (Wt Pct)	Al (Wt Pct)	P (Wt Pct)	*B* (ppm)
DP450B	0.04 to 0.07	1.1 to 1.4	0.03 to 0.05	0.01 to 0.03	>20
DP600B	0.10 to 0.13	1.4 to 1.7	0.03 to 0.05	0.01 to 0.03	>20
DP450P	0.10 to 0.13	1.1 to 1.4	0.03 to 0.05	0.06 to 0.1	>20
DP600P	0.13 to 0.16	1.4 to 1.7	0.03 to 0.05	0.06 to 0.1	>20
DP450Al	0.04 to 0.07	1.1 to 1.4	0.8 to 1.0	0.01 to 0.03	—
DP600Al	0.10 to 0.13	1.4 to 1.7	0.8 to 1.0	0.01 to 0.03	—

Engineering stress-strain curves for DP450 and DP600 specimens annealed at 800 ℃ cooled at a rate of 26 ℃/s are shown in Fig. 2.12. It was observed that DP600P and DP450P steels gave highest yield and tensile strength, which was due to the solid-solution strengthening effect of phosphorus. These steels also showed discontinuous yielding behaviour. The addition of aluminium lowered the amount of austenite formed, consequently lowered the amount of hard phases in the ferrite matrix. The Hollomon and Pickering parameters were determined by fitting the true stress-true strain data with Eq. (2.1) and Eq. (2.2), respectively.

$$\sigma = k\varepsilon^{n} \qquad \text{..... (2.1)}$$

$$\sigma = A + B(\varepsilon - \varepsilon_0) + C\mathrm{In}(\varepsilon - \varepsilon_0) \qquad \text{..... (2.2)}$$

It was found that the prediction ability of the Pickering model is higher than the Hollomon model, but Hollomon model is simple, as it involves only two parameters.

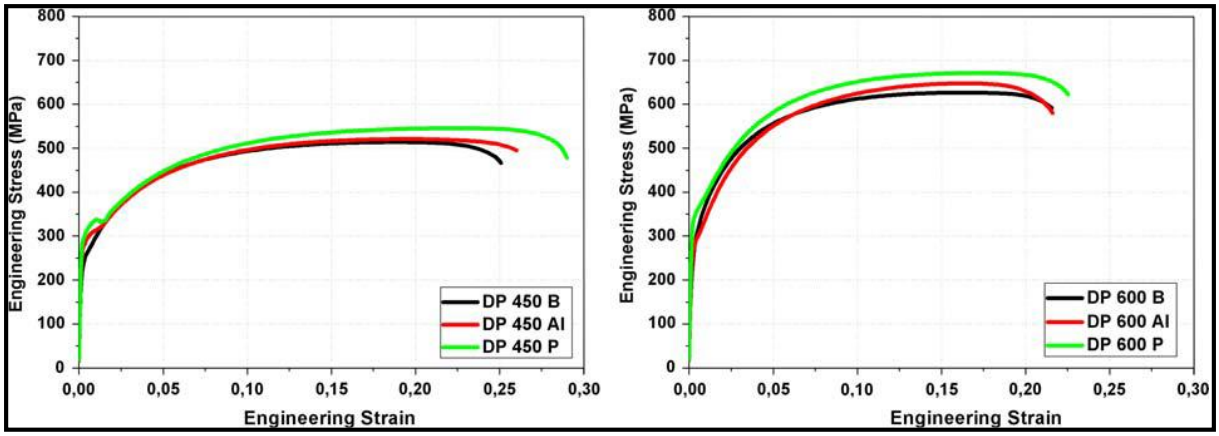

Figure 2.12: Stress-strain curves for DP450 and DP600 DP steel intercritically annealed at 800℃ and cooled at 26 ℃/s [59].

Das *et al.* [60] studied the effect of strain rate (0.001–800 s^{-1}) on the properties and micro-mechanisms of deformation of DP600 and DP800 steels having 10.2 % and 33.2 % martensite volume fractions respectively. UTS and YS for both the steels increased with increase in the strain rate. SEM and TEM were used to understand the deformation mechanisms. SEM micrographs displaying the micro-mechanisms of deformation at different strain rates are shown in Fig. 2.13. De-cohesion of ferrite–martensite interface was responsible for void initiation in case of DP600 for the whole strain rate range. In case of DP800 steel, de-cohesion of ferrite–martensite interface and micro-cracks in martensite were responsible for micro-void initiation at quasi-static strain rates. However at higher strain rates (800 s^{-1}), micro-voids were found to be initiated only due to de-cohesion of ferrite–martensite interface. It was reported from the TEM observations, that under quasi-static strain rates, deformation took place in ferrite matrix for both the steels. At higher strain rates, both ferrite and martensite deformed in case of DP800 whereas only ferrite matrix deformed in case of DP600. Crussard-Jaoul (C-J) analysis was done to study the strain hardening behaviour of both the steels under quasi-static conditions. Both the steels showed three stages of strain hardening. The stage 1 having higher slope than stage 2, represented the phase of dislocation generation at grain boundaries of ferrite after the yield point. In stage 2, movement and rearrangement of dislocations lowered the slope. This process of rearrangement of dislocations to form dislocation cells with the application of strain was called dynamic recovery. The stage 3 at higher strains was due to the onset of martensite deformation.

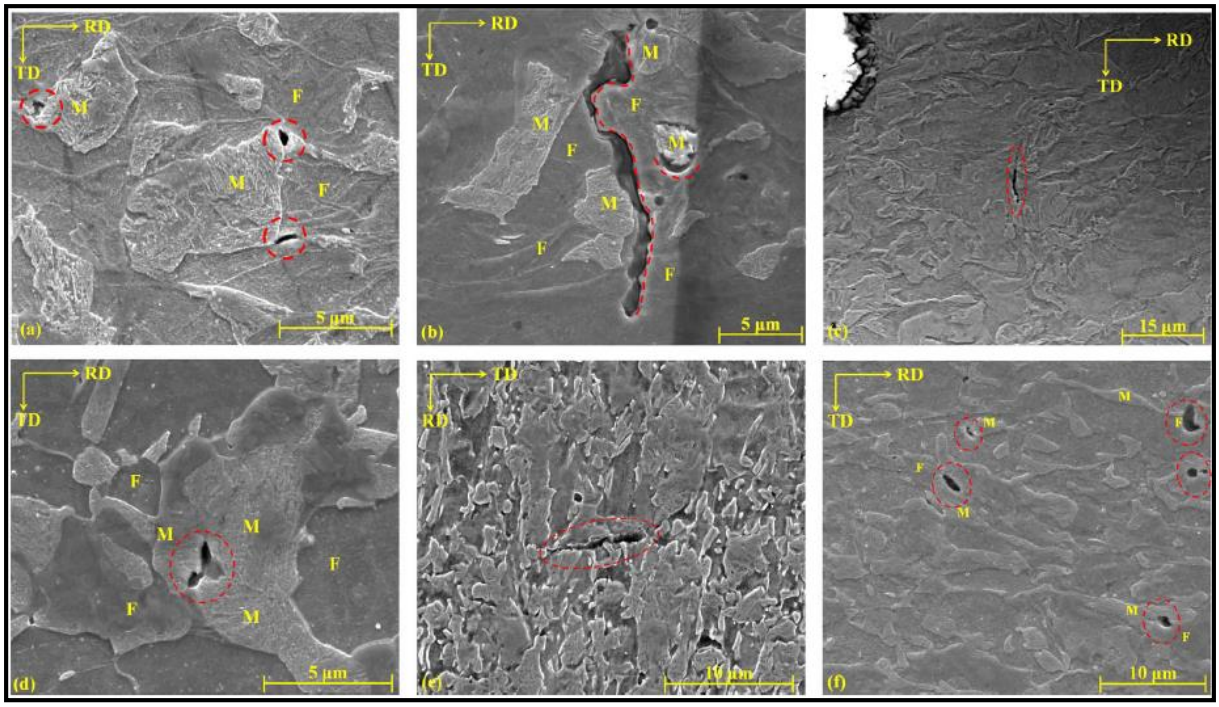

Figure 2.13: Microstructure on the transverse perpendicular plane adjacent to the fracture surface showing voids and cracks originated in DP600 steel at (a) 0.001, (b,c) 800/s, and in DP800 steel at (d, e) 0.001, (f) 800/s strain rates. M: Martensite, F: Ferrite [60].

Kim and Lee [61] studied the effect of martensite volume fraction and morphology on the behaviour of dual phase steels under dynamic (1750 s^{-1}) and quasi-static strain rates (10^{-4} s^{-1}). The chemical composition used was 0.21C-0.21Si-0.72Mn-0.01P-0.01S-1.1Cr-Fe (wt. %). Two different annealing cycles were used to get the dual phase steels with different martensite morphologies and volume fractions. In one case (referred as SQ, Step quenching), specimens were heated to 1000 ℃ for one hour and then held in intercritical region, followed by quenching to room temperature. In other cycle (referred as IQ, intermediate quenching), specimens were directly heated in the intercritical region and then quenched. Four specimens (two for each cycle) were prepared by varying the intermediate holding temperature. In IQ samples, fine fibrous martensite was uniformly distributed in the ferrite matrix, but in case of SQ samples, bulkier martensite was formed. Torsional kosky bar was used to conduct the torsional tests under quasi-static and dynamic strain rates. The test data was also correlated with microstructure and fracture surfaces. IQ annealed samples showed ductile fracture at quasistatic and dynamic strain rates, but the fracture mode of SQ specimens was changed from cleavage fracture to ductile fracture with change of strain rate from quasi-static to dynamic strain rates. It was reported that this change of fracture mode was due to softening of martensite due to adiabatic heating at higher strain rates. The maximum shear stress was found to increase with increase in the martensite volume fraction having the same

morphology. SQ specimens showed higher shear stress than IQ specimens having the same martensite volume fraction.

Wang *et al.* [41] studied the strain rate sensitivity of DP600, DP800, DP1000, and martensitic steel (MS1200) by using a split Hopkinson tensile bar (SHTB) and compared their properties with each other. The chemical composition of steels was as shown in Table 2.9. All the DP grades showed increase in tensile strength with increase in strain rate, but the increment in strength was decreased with increase in martensite fraction as shown in Fig. 2.14.

Table 2.9: Chemical composition of DP steel sheets and M1200 steel sheets (wt. %, Fe balance) [41].

Steel (thickness, mm)	C	Si	Mn	P	Cr	Ni	Al	Co	Nb	Cu	V
DP600 (1.2)	0.13	0.2	1.5	0.01	0.02	0.039	0.04	0.019	0.015		
DP800 (1.5)	0.13	0.2	1.49	0.03	0.02	0.037	0.04	0.019	0.016	0.008	0.02
DP1000 (1.0)	0.16	0.5	1.48	0.04	0.02	0.036	0.06	0.019	0.02	0.005	0.014
M1200 (1.0)	0.2	0.2	1.3	0.01	0.02	0.035	0.04	0.019	0.015	0.008	0.012

The strength of MS1200 steel decreased with increase in strain rate. Total elongation of DP600 and DP800 decreased with increase in strain rate, whereas the elongation of DP1000 and MS1200 was increased with increase in strain rate. It was reported that there are two opposing effects, work hardening and work softening due to the adiabatic temperature rise during high strain rates.

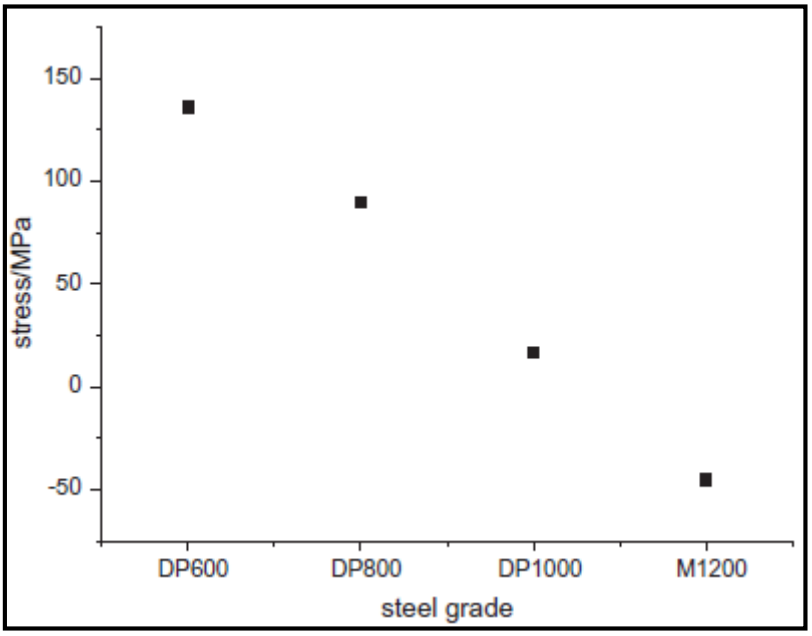

Figure 2.14: The increment in tensile strength of the four steel grades between the strain rates of 10^3 s^{-1} and 10^{-3} s^{-1} [41].

Work hardening is dominant at lower strain rates and work softening has more effect on steels having large amount of martensite at high strain rates. The decrease in strength of MS1200 and increase in the elongation of DP1000 and MS1200 was due to the adiabatic softening effect at high strain rates. The fracture analysis indicated that, DP600 and DP800 had ductile fracture both under quasi-static and high strain rate conditions and the fracture mode of DP1000 and MS1200 changed from cleavage fracture to ductile with change in strain rate from quasi-static to high strain rate.

Huh *et al.* [62] investigated the dynamic deformation behaviour of TRIP and DP steels at intermediate strain rates of 0.003 to 200 s^{-1}. Furthermore, the effect of pre-strain on the mechanical properties of TRIP600 and DP600 were studied at strain rates of 0.003, 1, 10, and 100 s^{-1}. High speed material testing machine was used to perform the tensile tests at intermediate strain rates. The material properties such as strain rate sensitivity, flow stress, work hardening rate, and fracture elongation were obtained from the tensile test data. The flow stress of each material was increased with increase in strain rate. The strain rate hardening of DP steels was higher than the TRIP steels.

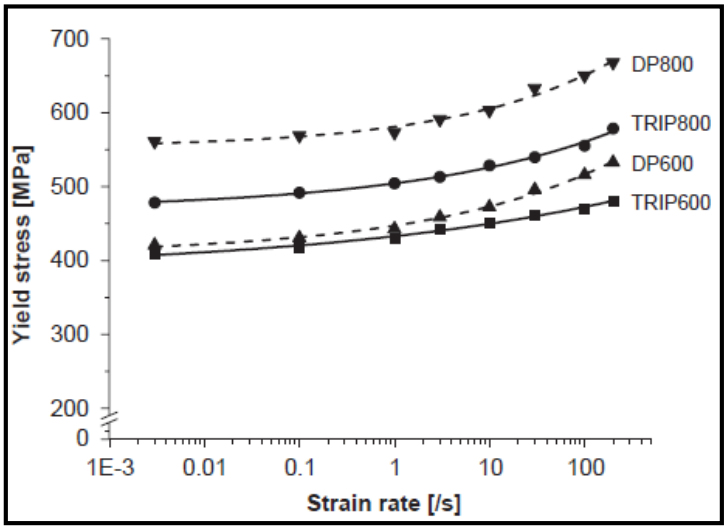

Figure 2.15: Yield stresses of TRIP-type and DP-type steel sheets at various strain rates [62].

The work hardening rate of each material decreased gradually with increase of true strain and the work hardening of DP steels was higher than the TRIP steels. The increase in yield stress with increase in strain rate was as shown in Fig. 15. It can be seen that DP600 and DP800 have more strain rate sensitivity than TRIP600 and TRIP800 steels. The fracture elongation of TRIP600 and TRIP800 was first decreased with increase in strain rate from 0.003 to 0.1 s^{-1} and then increased with increase in strain rate. The fracture elongation of DP steels increased

monotonically with increase in strain rate, and the fracture elongation of TRIP steels was higher than DP steels. The flow stress and ultimate tensile strength was increased with increase in pre-strain.

Kumar *et al.* [63] studied the effect of controlled austenite decomposition on the microstructure evolution in dual phase steels. The chemical composition of steel used is shown in Table 2.10.

Table 2.10: Chemical composition of steel in wt. % [63].

C	Mn	P	S	Si	Al	Cr	N
0.091	1.86	0.014	0.007	0.47	0.038	0.017	0.0035

Hot dip process simulator (HDPS) was used for simulation of different annealing cycles and SEM was used for microstructure characterization. The steel sheets was first austenitized at different temperatures (1000, 1050 and 1100 ℃), followed by intercritical holding at 800 ℃ for the decomposition of austenite and then ultra fast cooling to transform austenite to martensite. SEM micrographs revealed the formation of ferrite channel network around the boundaries of previous austenite grains as shown in Fig. 2.16. It was observed from the fracture tip analysis, that micro-cracks initiated in the lath martensite were arrested in the surrounding ferrite.

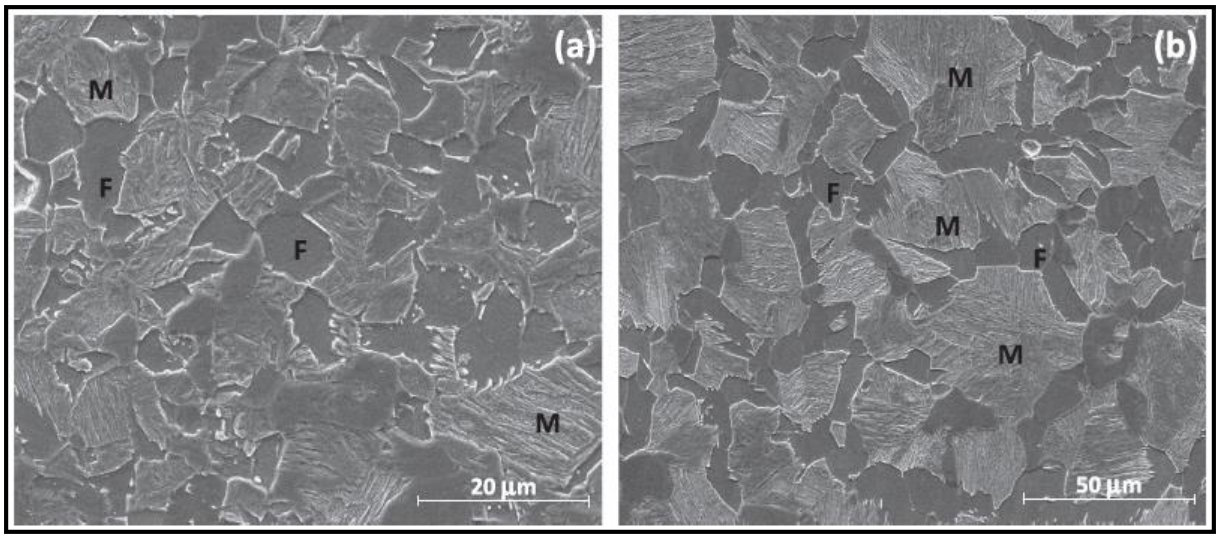

Figure 2.16: Microstructure evolution showing dual phase formation by the annealing process (a) at 1000 °C and ferrite channel formation (b) at 1100 °C [63].

This phenomenon assisted in delaying the onset of global deformation and hence increased the ductility. The fractography of the fractured surfaces after tensile testing was done to understand the fracture mode of the different specimens, austenitized at 1000, 1050 and 1100 ℃. All the specimens showed mixed mode of fracture having cleavage and ductile

fracture to varying degree. Fracture surface of specimen austenitized at 1000 ℃ showed more cleavage fracture having some dimples, indicating lack of ductility. But the other two specimens, showed dimple area surrounding the cleavage fractures of martensite. This area was more in case of samples austenitized at 1100 ℃, which indicated the increase in ductility in this case.

Hao *et al.* [64] performed dynamic (500 s^{-1}) and quasi-static tensile tests ($5.6x10^{-4}$ s^{-1}) on a quenching-partitioning-tempering (Q-P-T) martensitic steel with high amount of retained austenite (RA). Similar tests were also performed on a simple quenching and tempering (Q&T) steel with little RA to analyse the influence of presence of RA on the performance of steels. For Q-P-T steel, there was increase in strength with small drop in percentage elongation under dynamic conditions as compared to quasi-static conditions (see Fig. 2.17). For Q&T steel, there was increase in both strength and percentage elongation with increase in strain rate. However, the total elongation (16.8 %) and product of strength and elongation (21,420 MPa%) of Q-P-T steel were much higher than the total elongation (10.4 %) and product of strength and elongation (14,706 MPa%) of Q-T steel. The product of strength and elongation (which is a measure of impact toughness) increased by 2169 MPa% for Q-P-T steel on shifting from quasi-static to dynamic testing conditions. In dynamic testing, there are two conflicting effects viz. (i) strain rate hardening of martensite, and (ii) adiabatic softening of martensite. In the early phase of deformation, strain rate hardening pre-dominates which gives high strength at high strain rates. However, in further deformation prior to fracture, adiabatic softening of martensite pre-dominates which provides higher elongation than in case of quasi-static tensile tests. Thus, both strength and ductility increased in case of Q-T steel. In case of Q-P-T steel, there was increase of strength due to strain hardening of martensite in the initial stages of deformation. During subsequent deformation, softening of martensite due to adiabatic heating led to increased percentage elongation. However, this increase in elongation could not effectively compensate the loss of ductility (elongation) due to suppression of DARA effect during high strain rate testing. Thus, there was a slight loss of ductility at high strain rate testing compared to quasi-static conditions. The suppression of DARA effect was proved by XLPA study (X-ray diffraction line profile analysis) of dislocation density in martensite of fractured samples of Q-T and Q-P-T steels under dynamic strain rates.

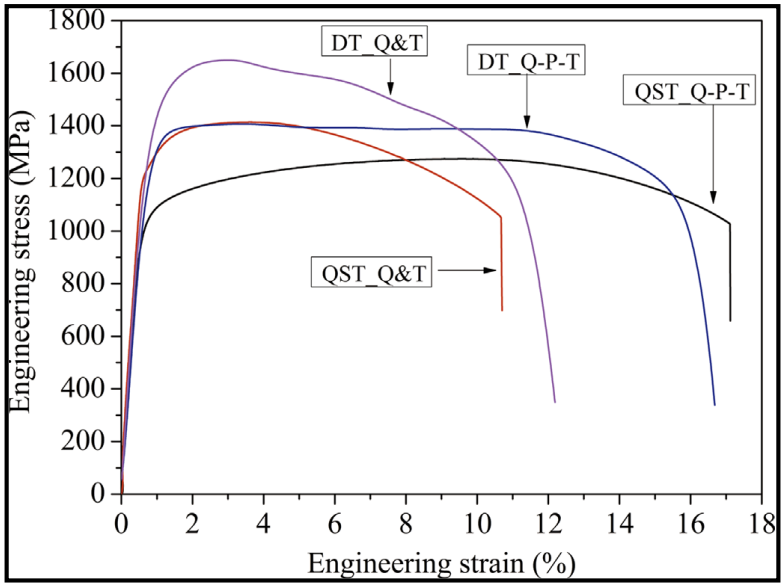

Figure 2.17: The engineering stress-strain curves of the quasi-static and dynamic tensile tests of the Q-P-T and Q&T samples [64].

It was observed that loss of dislocation densities in martensite was approximately same for both the steels due to adiabatic softening of martensite during dynamic testing. This showed that at higher strain tares, DARA effect was not active. This is because if DARA effect was present, then the loss of dislocation densities in martensite should have been much more in Q-P-T steel as compared to Q-T steel.

2.3 Summary of literature

- Several authors have studied the effect of high strain rate on the mechanical properties of DP steels. It was observed, that strength values generally increase and uniform elongation decreases with increase in strain rate [1, 28, 41, 53, 58, 60, 61, 64]. Some authors have reported about different equipment used for testing at higher strain rates [56, 57].
- A few authors have studied the effect of pressing of sheet (pre-straining) and paint bake cycle (bake hardening) employed during the manufacturing process of automotive body structures, on the mechanical properties of DP steels at quasi-static and high strain rates. Tensile strength and yield strength increased whereas elongation decreased subsequent to these treatments [40, 62].
- Some authors have studied the effect of carbon content on the microstructure and mechanical properties of DP steels. With increase in carbon content in DP steels, the volume fraction of martensite was increased and consequently, the strength was increased [54, 55].

- A few authors have investigated the effect of change in temperature on the mechanical properties of DP steels at different strain rates [40, 52].

2.4 Gaps in the reviewed literature

- Although, a few authors have studied the influence of second phase martensite volume fraction, morphology, and distribution on mechanical properties of DP steels under quasi-static strain rates, limited literature is present on its effect on the mechanical properties of DP steels under high strain rate dynamic conditions. Further, ferrite-bainite dual phase steels have not been investigated much for their mechanical properties under high strain rate testing conditions.
- The effect of change of temperature on the high strain rate properties of DP steels having different martensite distribution, morphology, and volume fraction have not been investigated much.
- Most of the authors have attempted to improve the mechanical properties of ferrite-martensite DP steels by varying the martensite volume fraction and carbon content in martensite. However, limited research is available showing the influence of ferrite-martensite interface morphology and special distribution on the mechanical properties of DP steels under quasi-static and high strain rate conditions.

Chapter 3
Design of the Study

3 Design of the Study

3.1 General

The chapter presents the formulation of research objective in the light of limitations in the existing literature. The chapter also discusses the details of the starting material used for the present research work, the key issues, general methodology and experimental procedure used in the research work. Finally, the equipment used for experimentation have been discussed.

3.2 Establishment of objective function

DP steels are the most commonly used AHSS grade in the manufacturing of automobile components and parts. DP steels consists of a soft ferrite matrix having hard phase martensite. Ferrite grain size, martensite volume fraction, morphology and spatial distribution are the critical factors which influence the properties of DP steels. DP steels with different properties viz. yield strength, ultimate tensile strength, and elongation etc. can be obtained by tailoring these factors. Some researchers have studied the influence of martensite volume fraction, morphology and distribution on the properties of dual phase steels under quasi-static strain rates [44, 55, 65–68]. Some researchers have studied the influence of change in martensite volume fraction at high strain rates by taking different DP grades having different amount of alloying elements [28, 41, 58, 60]. Scant literature is present on the influence of change in martensite volume fraction, morphology and spatial distribution (without change in alloying elements) on the high strain rate properties of low carbon DP steels. For automobiles, better properties are compulsory during crash conditions for the safety of passengers. The present study is an attempt to understand the effect of martensite volume fraction, morphology, and distribution on the properties (especially under high strain rates) of DP steels.

In the present work, three different annealing cycles were used to get distinct DP microstructures having different martensite morphology, distribution, and volume fraction. One cycle (CAL: continuous annealing line) was employed to get the conventional DP grade used in industry and one (CHCL: continuous heating and cooling line) was used to get different distribution of martensite having same amount of volume fraction as in CAL cycle. The DP microstructure processed with CHCL cycle had large amount of in-grain martensite

in the ferrite matrix than in DP grade obtained by CAL cycle. Third cycle (CAS: core and shell) was used to get DP microstructure with large amount of martensite and having core-shell like microstructure. In this DP microstructure martensite grains were surrounded by the channel like network of ferrite.

The main objective of the present research work was to study the effect of martensite distribution, morphology, and volume fraction on the mechanical properties of DP steel under quasi-static ($2.7 \times 10^{-4}\ s^{-1}$) and high strain rate conditions ($100–650\ s^{-1}$).

3.2.1 Key issues to be taken up during the research work:

(i) To determine the microstructure of the as-received 67 % cold rolled low carbon steel by using the optical microscopy.

(ii) To process the as received samples by different annealing cycles, to get DP microstructures having different volume fraction, morphology, and distribution of martensite. The three different annealing cycles used were (i) conventional industrially used CAL cycle (ii) CHCL cycle to get different distribution of martensite in ferrite matrix (iii) CAS cycle to get large fraction of martensite having martensite grains surrounded by ferrite network.

(iii) To obtain the phase fraction of each phase present in the three distinct microstructure with the help of image analyzing software 'ImageJ'.

(iv) Evaluation of the mechanical properties of different specimens under quasi-static strain rate condition of $2.7 \times 10^{-4}\ s^{-1}$.

(v) To analyze fractographs of fractured surfaces and microstructures of the fracture tips to analyse the micro-mechanisms of deformation under quasi-static conditions.

(vi) To repeat steps [(ii)–(v)] for high strain rate testing conditions. Testing at 100, 200 500 and 650 s^{-1} was done using high speed servo-hydraulic Instron VHS 8800 test system.

(vii) To analyse the data obtained from quasi-static and high strain rate testing and compare the results obtained at different strain rates.

3.3 Experimental procedure

The experimental procedure followed during the research work is described in this section.

3.3.1 Starting material

An industrially processed 67 % cold rolled sheet with a final thickness of 0.83 mm and a lean chemical composition as shown in Table 3.1 was used in this study. The standard metallographic techniques were used for the microstructure characterization of the as received steel. The rough polishing was done by using emery papers and then fine polishing was done with alumina powder and water by using cloth polishing machine. 2 % Nital was used to reveal the grain boundaries of different phases present in the microstructure. The microstructure was obtained by using optical microscope.

Table 3.1: Chemical composition of the as-received steel used in the present work.

Element	C	Mn	P	S	Si	Al	N
(wt. %)	0.074	1.83	0.012	0.002	0.43	0.026	0.0032

3.3.2 Annealing simulations

After evaluation of the starting material, the next step was to determine the process parameters for the three different annealing cycles for obtaining required DP microstructures having different morphology, distribution, and volume fraction of martensite. The annealing parameters including upper and lower critical temperatures, heating rates, cooling rates, and inter-critical holding time and temperature for the two cycles (CAL and CHCL) were selected from the existing literature [67, 68]. The third cycle (referred here as CAS) was obtained by some modifications in the annealing cycles reported by Kumar *et al.* [63]. The three annealing cycles were conducted in a HDPS (hot dip process simulator) as shown in Fig. 3.1. These annealing cycles are described in the following sub-sections.

3.3.2.1 CAL cycle

Continuous annealing line (CAL) cycle used in the present work was similar to the conventional cycle used in the industry. In this cycle, specimens were heated to 790 ℃ by using heating rates of 10 ℃/s followed by isothermal holding at this temperature for 60 s as shown in Fig. 3.1. Inter-critical holding was done for the transformation of pearlite, nucleation and grain growth of austenite. After that cooling was done in three stages discussed below.

i. The first stage was slow cooling from 790 ℃ to 675 ℃. This stage of slow cooling resulted in the carbon enrichment of austenite and ferrite transformation.

ii. The second stage was fast quenching up to 275 ℃ for the transformation of austenite to martensite. Fast cooling rate (40 ℃/s) was used to avoid the formation of bainite.

iii. The third stage was holding at 275 ℃ for 120 s for the tempering of transformed martensite. Tempering was done to get the DP steel with improved ductility.

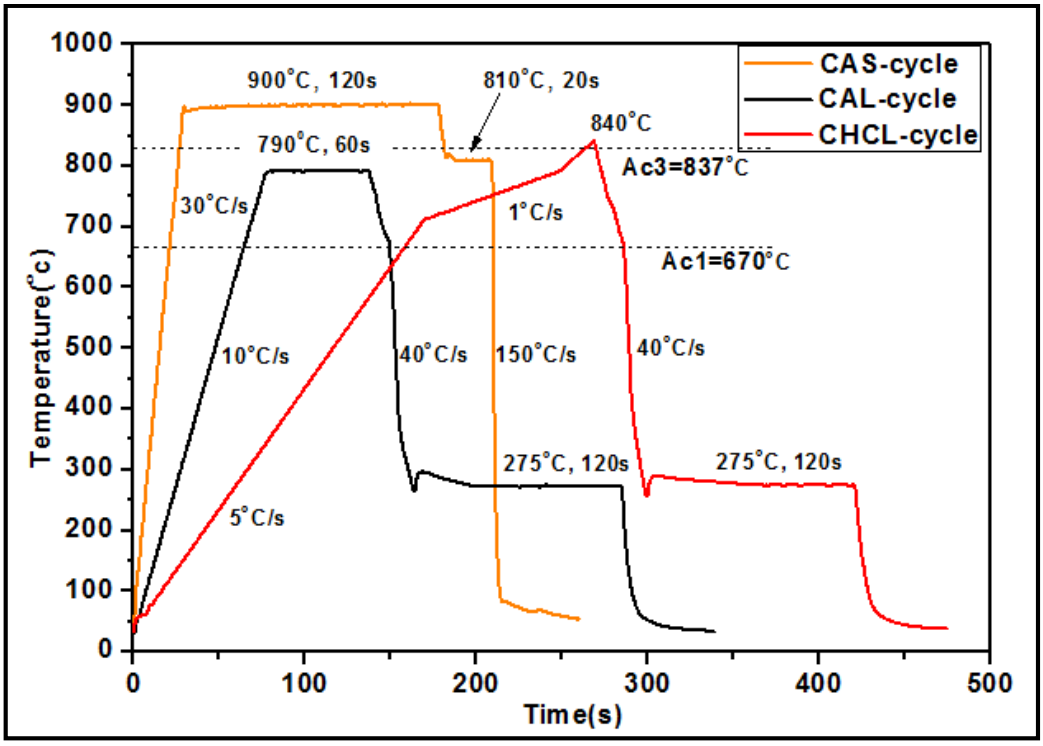

Figure 3.1: Three different annealing cycles including CAL, CHCL, and CAS used in the present work.

3.3.2.2 CHCL cycle

The continuous heating and cooling line (CHCL) cycle was obtained by modifications in the heating stage of the conventional annealing cycle (CAL cycle) as shown in Fig. 3.1. This was done to get DP microstructure with variations in distribution and morphology of martensite but having same volume fraction of martensite as obtained by CAL cycle. In the CHCL cycle heating was done in three stages. In the first stage, heating was done up to 710 ℃ by using heating rates of 5 ℃/s. This slow heating rate was used to get more recrystallization of ferrite and better dispersion of cementite/carbides present in pearlite before entering into the inter-critical region. In the second stage, heating was done up to 790 ℃ with more slow heating rate of 1 ℃/s. This stage allowed further recrystallization of the remaining grains and growth of the already formed ferrite grains. In this stage, austenite grains also started nucleating. The nucleation of austenite was expected to occur at the uniformly dispersed carbides because of the presence of high carbon concentration at these locations. The better dispersion of carbides

which promoted austenite nucleation at these sites, was mainly the reason for in-grain distribution of the martensite. In this cycle, holding at 790 ℃ was eliminated, because it was anticipated that it could lead to grain growth of austenite. So, further heating up to 840 ℃ was done with heating rate of 2 ℃/s. This temperature was selected to get same amount of austenite (as was obtained in CAL) and without any grain coarsening. Finally, the cooling was done by using similar stages as used in the conventional CAL cycle.

3.3.2.3 CAS cycle

The CAS cycle (CAS name was given as it provided core and shell type DP microstructure) described in Fig. 3.1 was obtained by some modifications to the annealing cycle as reported by Kumar *et al.* [63]. The modifications include change in austenitizing temperature from 1100 ℃ to 900 ℃ and time from 60 s to 120 s, change in inter-critical holding temperature from 790 ℃ to 810 ℃. The objective of this cycle was to obtain core and shell like DP microstructure to analyze its effect on the properties of DP steel at high strain rates. In this cycle, fast heating rate 30 ℃/s was used to inhibit the recrystallization of ferrite. The austenitizing was done at 900 ℃ for 120 s for nucleation and grain growth of austenite. After this, rapid cooling was done to 810 ℃ followed by intercritical holding of 20 s. This was done for nucleation of ferrite around austenite grains to form ferrite channel network. After this, ultra-fast cooling rates of 150 ℃/s was used for cooling the steel to room temperature. The complete transformation of austenite to martensite was obtained by using ultra-fast cooling rates.

Therefore, by heat treating the as-received steel samples by using above discussed three different annealing cycles, it was possible to get DP microstructures with different martensite volume fraction, morphology, and distribution. This was the required input to analyze the effect of these different DP microstructures on the properties under quasi-static and at high strain rates, which was the main focus of the research work.

3.3.3 Tensile testing at quasi-static strain rates

For tensile testing under quasi-static conditions, specimens were prepared according to ASTM standard E-8M. After annealing, the samples were tested by using an INSTRON 8862 servo-hydraulic machine having load capacity of 100 kN. A 25 mm gauge length extensometer was used to measure the strain values and the cross head extension speed used was 0.5mm/s which provided strain rate of 2.7×10^{-4} s^{-1}. Load (kN) and strain (%) values

were obtained from this machine and the engineering stress was obtained by dividing the load values by cross-sectional area of the tested specimen measured before testing.

3.3.4 High strain rate testing

The procedure followed for high strain rate testing at strain rates of 100, 200, 500, and 650 s^{-1} is described in the following sub-sections. The sample used for high strain rate testing is shown in Fig. 3.2.

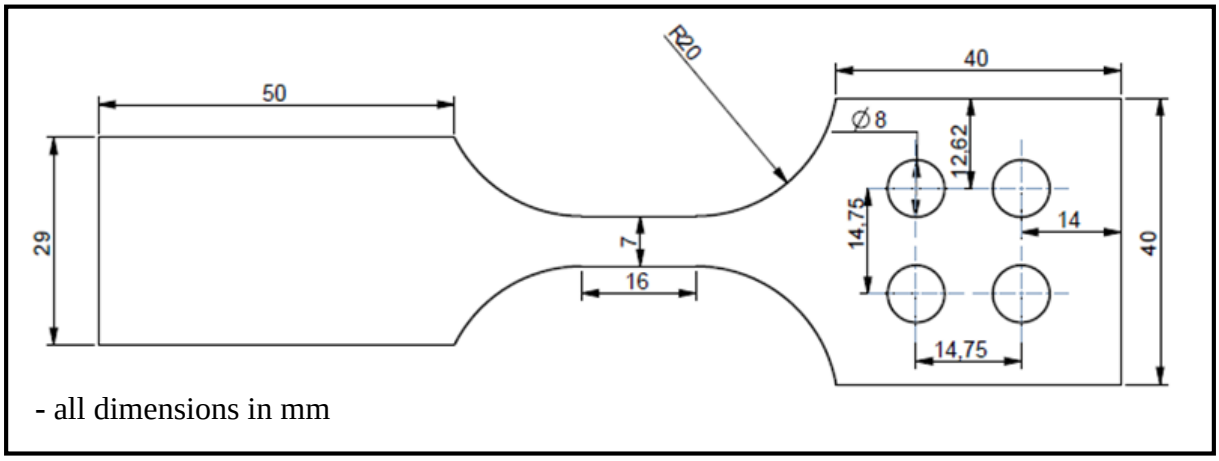

Figure 3.2: Schematic drawing of sample for high strain rate testing.

3.3.4.1 High strain rate testing at strain rates of 100 and 200 s^{-1}

The annealed samples were tested at strain rates of 100 and 200 s^{-1} by using High-speed servo-hydraulic test system having capacity to obtain displacement velocities up to 20 m/s. The piezoelectric load cell and LVDT (linear variable differential transformer) extension gauges available in the test system were used for the load and extension measurements respectively. The data obtained by this system contained some noise as shown in Fig. 3.3; this noise level increased with increase in strain rate. This data was smoothened by using origin software as shown in Fig. 3.3.

3.3.4.2 High strain rate testing at strain rates of 500 and 650 s^{-1}

It was not possible to get accurate data from the load cell and extension gauges available in the system at high strain rates. Therefore, seperate strain gauges (Make: Kyowa Electronic Instruments Co. Ltd., Japan) were utilized and pasted directly on the samples to get accurate and smooth data under high strain rate testing conditions. The strain gauges and material required for pasting strain gauges on the sample were as follows.

- Strain gauge for load measurement was a roset designated as KFG-2-120-D16-23 having 2 mm gauge length and 120 Ω resistance. Two gauges were used for one sample.
- Strain gauge used for strain measurement was designated as KFEM-5-120-C1-11 having gauge length of 5 mm and 120 Ω resistance. One gauge was used for one sample.
- Glues designated as CC-33A and CC-36 were used for pasting of strain gauge for load and strain measurement respectively.

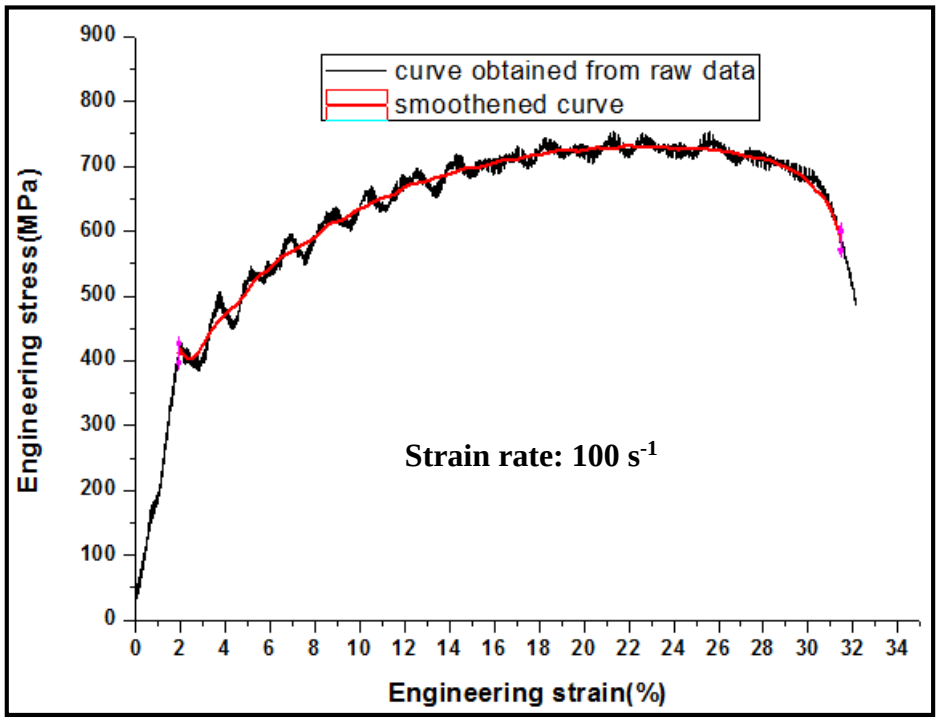

Figure 3.3: Smoothening of raw data obtained from the high strain rate testing machine.

Additionally, the following points were taken care of, for sample preparation.

- Acetone was used to clean the surface of samples and to remove particles of grease or oil present on the surface of samples.
- Emery papers of three different grades viz. 220, 320, and 400 were used to ensure flatness of sample surface and get uniform rough surface for pasting of strain gauges.
- Dilute phosphoric acid solution (6 wt. % phosphoric acid, 94 wt. % distilled water) was used to clean the metallic particles after paper polishing. It cleans the surface by reacting with the metallic particles.
- A neutralizer was used to neutralize the acidic surface of the sample. The chemical composition consisted of ammonium hydroxide (0.02 wt. %), trisodium phosphate

(0.05 wt. %), sodium tetrabonate pentahydrate (0.01 wt. %) and distilled water (99.92 wt. %).

- Cotton swaps were used to clean the acidic and neutralizer solutions.
- Bondable terminals were used to make the connections in strain gauges to complete the wheatstone bridge circuit.
- Soldering unit was used to solder and connect the three strain gauges to complete wheatstone bridge circuits.

3.3.5 Procedure to prepare high strain rate sample

The sample was placed on a glass sheet cleaned with acetone. The sample was cleaned with acetone to remove all the dust, grease or oil present on the surface of sample. The sample was mounted on the glass sheet to restrict its movement during polishing. Three gauges were pasted on one sample. The strain gauges for load measurement were pasted (one on each side of the sample) on the sample area which experiences only elastic forces (i.e. outside the gauge length area having larger width and no holes; see Fig 3.2 and Fig. 3.4). The second strain gauge for load measurement was pasted on the other side of sample but at the same location. Now, marking was done at 30 mm from the specimen edge (where sample width was 29 mm) with a cutter as shown in Fig. 3.4. Now a line parallel to the axis of the sample (marked as axial line) was drawn at the middle of the previous line (marked as, line for reference at 30 mm) as shown in Fig. 3.4. These lines are drawn to allot a specific position to the strain gauges so that the other strain gauge is pasted on the back side of the sample at the same position by following the same marking procedure. After deciding the locations on sample for pasting strain gauges, cleaning and polishing of the selected areas on the sample was done as follows. The polishing was done with 220 emery paper with the direction of polishing along the tensile axis of the specimen. Then 320 emery paper was used to polish in the transverse direction and again 400 emery paper was used to polish in the axial direction. The polishing direction was chosen so that the final polishing direction would be along the axial direction of the specimen. Now after this acidic solution was applied on the polished area to clean the metallic particles and then cleaned with cotton swaps. After this, neutralizer was applied to neutralize the surface and cleaned with cotton swaps. Now this area was ready to paste the strain gauges. The strain gauges were first pasted with the help of a transparent tape so that the marked lines were visible. Now, the tape was removed from one side up to the strain gauge and the CC-33A glue was applied on the bottom of the gauge. Now the tape was again pasted by applying some pressure from the pasted side to squeeze extra amount of

glue below the strain gauge. After this the tape was allowed to stay there for 10–20 minutes and then the tape was slowly and carefully removed so that the strain gauge will remain pasted on the sample as shown in Fig. 3.4. The same procedure was followed for the second strain gauge to be pasted on the other side of the sample. Similar procedure was followed for pasting the strain gauge for strain measurement on the gauge area of the specimen. There were no requirements of marking, but care was taken so that the axis of the strain gauge is parallel with the axis of the sample as shown in Fig. 3.5. CC-36 glue was used for pasting of strain gauge.

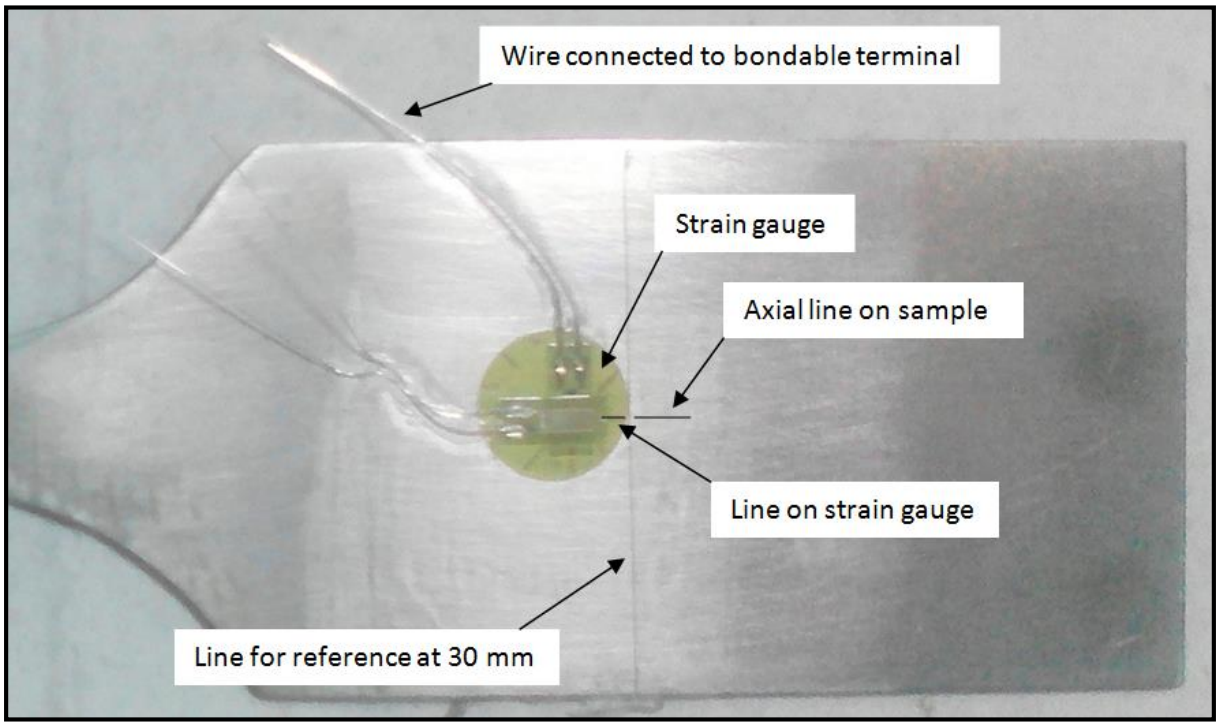

Figure 3.4: Position and alignment for pasting of strain gauge for load measurement.

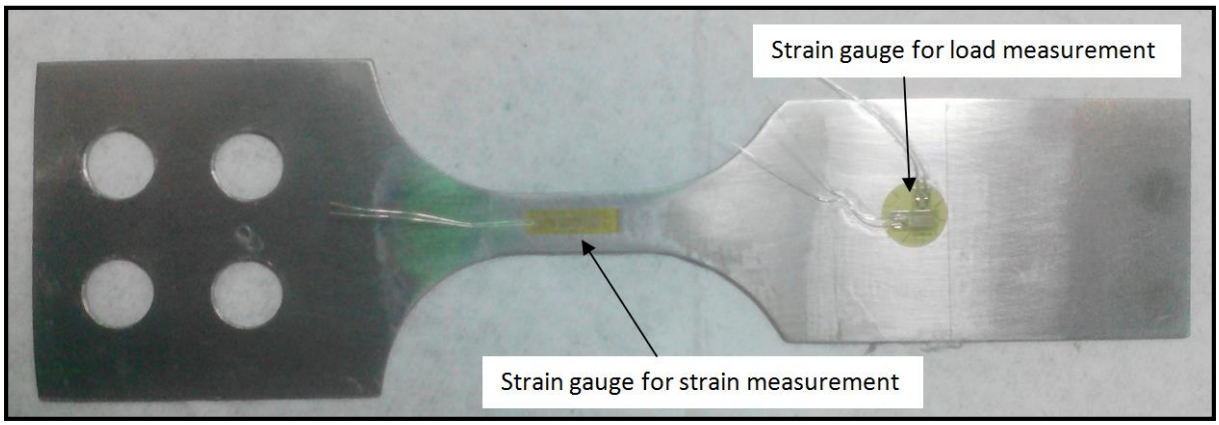

Figure 3.5: Two strain gauges pasted on reverse side of sample.

3.3.5.1 Making connections of strain gauges

The two strain gauges pasted on the tensile sample for load measurement were connected in a half bridge connection on the sample itself. The other half of the wheatstone bridge was in the machine system. To complete the wheatstone bridge circuit, both the halves were connected by wires. Bondable terminals and soldering unit were used to make the connections. For the strain gauge pasted for strain measurement, quarter bridge connection was made on the sample and this was connected to the remaining part of the wheatstone bridge in the system to complete the circuit. These connections are shown in Figure 3.6.

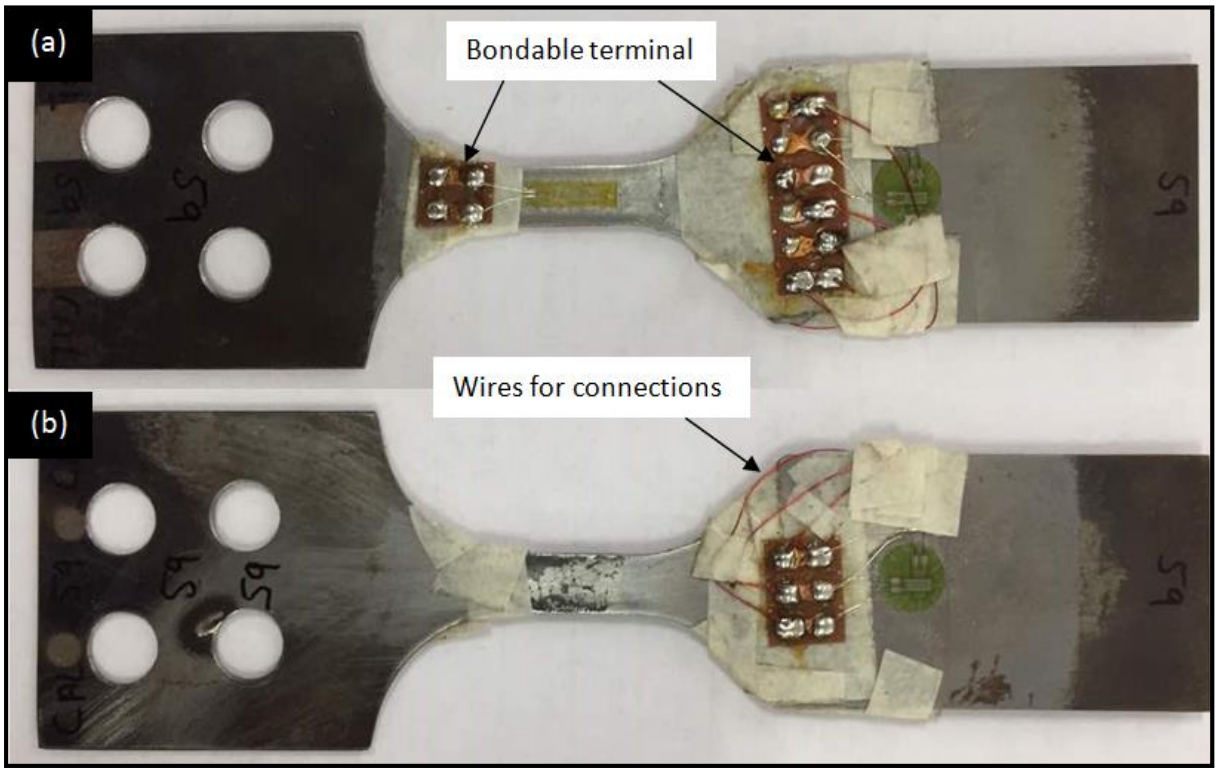

Figure 3.6: Connections of strain gauges in the high strain rate sample showing (a) front side and (b) back side of sample.

3.3.5.2 Calibration of strain gauges

After making all the connections, the strain gauges pasted on the specimens were calibrated for each sample before the tensile testing on the high strain rate testing machine. The calibration of strain gauges was done using a simple UTS machine and an extensionometer of 12.5 mm gauge length. The specimen was mounted on the UTS machine and 0.5 kN load was applied by using the control panel of machine. Now to calibrate the strain gauges for load measurement, 20 kN was taken equal to 10 V output from the amplifier and accordingly 0.5 kN was set equal to 0.25 V output from the amplifier used for output of load measurements. The maximum capacity of strain gauge used for strain measurement was to measure 20 %

strain. So 20 % strain value was taken equal to10 V and accordingly for the strain output at 0.5 kN loading, the output for amplifier was calculated and set by rotating the knob of the amplifier. For example, in case of a specimen it was 0.0412 % and the equivalent voltage was 0.0206 V. This voltage was set as an output of the amplifier at 0.5 kN loading. In this way, all specimens were calibrated one by one and simultaneously tested on high strain rate testing machine.

3.3.6 Strain hardening behaviour

Modified Crussard–Jaoul (C–J) method based on Swift equation (see Eq. (3.1)) is generally used for analysing the strain hardening behaviour of DP steels [69–71]. In the present work, this method was used to analyse the strain hardening behaviour of steels (under quasi-static strain rate conditions) with different dual phase microstructures.

$$\varepsilon = \varepsilon_0 + k\sigma^m \qquad \text{.....(3.1)}$$

where ε,σ, m,ε_0, and k are the true strain, true stress, strain hardening exponent, initial true strain and material constant respectively. The logarithmic form of Swift equation (see Eq. (3.2)) is obtained by differentiating with ε.

$$ln\left({}^{d\sigma}/_{d\varepsilon}\right) = (1-m)ln\sigma - ln(km) \qquad \text{.....(3.2)}$$

The strain hardening behaviour of DP steels with ferrite-martensite based microstructure strongly depends on the volume fraction, morphology, and hardness of martensite phase [72, 73]. The strain hardening region of ferrite-martensite based DP steels comprises of (up to) three distinct stages [60, 72, 74, 75]. The first stage of higher strain hardening rate is due to presence of GNDs (geometrically necessary dislocations) and internal stresses generated in the microstructure due to austenite to martensite transformation during quenching [60, 72]. During this initial deformation stage, the dislocations interact with each other and also with martensite particles, thereby resulting in high strain hardening rate [60, 72]. Further, Bergstrom *et al.* [74] and Ashrafi *et al.* [75] reported that higher amount of martensite present in DP microstructure reduces the active participation of ferrite in deformation during this initial stage and consequently leads to high strain hardening during the first stage. During the second stage of strain hardening, the ferrite phase deforms plastically whereas martensite phase deforms elastically. Finally, in the third stage of strain hardening, plastic deformation of martensite phase takes place [60, 72].

3.3.7 Strain rate sensitivity

The variation in true stress values with strain rate at a given strain value is called strain rate sensitivity. The strain rate sensitivity of steels can be calculated using the relation as given by Eq. (3.3) [76].

$$m = \left[\frac{\partial \ln \sigma}{\partial \ln \dot{\varepsilon}}\right]_{\varepsilon} \quad \text{.....(3.3)}$$

here m, σ, ε, and ἐ are representing strain rate sensitivity, true stress, true strain, and strain rate respectively. Strain rate sensitivity value signifies the change in strength of a material with changes in strain rate. A positive value of strain rate sensitivity for a given strain range signifies that for the given strain range, any increase in strain rate results in increase in strength of the material at a given strain value.

3.3.8 Energy absorption capacity at various strain rates

The energy absorption capacity of a material is the most important property required for crashworthiness of vehicle body material and should be high to absorb crash energy during collision accidents. Some authors use the product of ultimate strength and total elongation (PSE) to represent the toughness property of the material [64, 77]. However, using this method, the calculated value of energy absorption is higher than the actual toughness of material (actual energy absorption intensity).Wang *et al.* [41] used a more accurate energy absorption method (Eq. (3.4)) to calculate toughness of samples (in GPa%) tested under different strain rates [41].

$$\Delta E = \int_0^{\varepsilon} \sigma d\varepsilon \quad \text{.....(3.4)}$$

Here, ΔE, σ and ε are energy absorption intensity, engineering stress, and engineering strain respectively.

3.4 Machines and equipment used

This section describes the various machines and equipments used in the present study.

3.4.1 Hot dip process simulator (HDPS)

HDPS set-up (Make: ICS Iwatani Surtec, Germany) was used for annealing simulations of three different cycles used in this study (see Fig. 3.7). This is a highly automated machine which can be used for galvanizing and annealing of sheet metal samples. It has infrared heating system with highest heating capacity up to 1200 ℃. The highest heating rate of 30 ℃/s and ultra-fast cooling rates of 150 ℃/s can be obtained in this system. The sample is

mounted on the end of a rod, which is operated by an automatic system. This rod moves in the heating and cooling chamber according to the requirements of the annealing cycle. A k-type thermocouple is directly spot welded on the sample to get accurate temperature values. A mixture of H_2 (10 %) and N_2 (90 %) was used to create an inert atmosphere to prevent oxidation of samples. The required annealing cycle (process route) was programmed and then the machine automatically worked according to the instructions given in the program. The sample was automatically moved in the heating and cooling chambers according to the requirements. In heating chamber, infrared heating system heated the sample to the required temperature with specified heating rate and in cooling chamber, controlled volume of gas mixture was supplied for the required cooling rate.

Figure 3.7: Hot dip process simulator used for annealing of samples.

3.4.2 Tensile testing machine for testing at quasi-static strain rate

The tensile testing machine (Instron 8501 System, *Instron Engineering Corporation*, Norwood, USA) with a loading capacity of 100 kN was used for tensile testing at quasi-static strain rate of 2.7×10^{-4} s^{-1} (see Fig. 3.8). The cross head displacement speed used was 0.5 mm/min. This system had a maximum capacity of 120 mm/min of displacement speed of crosshead. A 25 mm gauge length extensometer was used to get the strain values. The load

and strain data were obtained from this machine and then converted to stress-strain data by using origin software.

Figure 3.8: Tensile testing machine for testing at quasi-static strain rate.

3.4.3 Tensile testing machine for testing at high strain rates

High speed servo-hydraulic Instron VHS 8800 test system (Instron Engineering Incorporation, Norwood, USA) of 100 kN capacity and ability to obtain displacement velocities of up to 20 m/s was used to conduct high strain rate tensile tests (see Fig. 3.9). This system contained piezoelectric load cell and LVDT extension gauges to get the load and displacement data respectively. This system had provision to acquire data from external strain gauges used to get accurate and noise free data at high strain rates. For strain rates of 100 and 200 s^{-1}, the data obtained from piezoelectric load cell and LVDT extension gauges available in the test system was used for tensile plots. However, for still higher strain rates, it was not possible to get accurate data from this load cell and extension gauges. Therefore, for strain rates of 500 s^{-1} and 650 s^{-1}, separate strain gauges (Make: Kyowa Electronic Instruments Co. Ltd., Japan) were used to get noise free data. Strain gauge (KFG-2-120-D16-23) of 2 mm gauge length and 120 Ω resistance was used for measurement of load, and strain gauge (KFEM-5-120-C1-11) of 5 mm gauge length and 120 Ω resistance were used for

measurement of strain. Amplifiers were available to amplify the voltage signals obtained from the strain gauges and then sent to the system.

Figure 3.9: High speed servo-hydraulic Instron VHS 8800 test system for testing at high strain rates.

3.4.4 Facilities for sample preparation

The equipments used for preparation of samples for the microstructure characterization under optical microscope and SEM are discussed briefly in this section.

(a) Paper grinding

The sample surface to be examined by optical microscope and SEM were first polished with abrasive papers of grit size ranging from 80, 100, 220, 320, 400, 600, 800, 1000, 1200, 1500, and 2000 mesh size. Generally, polishing was started from 220 grade paper. 80 and 100 grade papers were used to remove large volume of metal from the surface if any. The polishing was started from the rough 220 paper and continued until all the scratch marks were in one direction. Then polishing is done on the next finer grade paper with polishing direction shifted perpendicular to the previous. Similarly, polishing was done up to the finest grade paper. The polishing should be done carefully to avoid deep scratches on the sample. The paper should be cleaned before polishing to remove the metallic particles and other contaminants.

(b) Cloth polishing

After paper polishing, cloth polishing was done on polishing machine (Make: BANIPOL METCO, Model No: PMV018, *Chennai Metco Pvt. Ltd.*, Chennai, India) to get mirror like smooth surface. A soft cloth (velvet, canvas, suede etc.) on rotating wheel was used to retain alumina or colloidal solution for polishing of the sample surface. The cloth was washed properly with water to remove all the contaminants to avoid scratches on the sample. After this, fresh alumina solution was applied on the cloth and then the sample was held on this rotating wheel to remove all the scratches. The cloth was again washed with water and then the polishing was done with water to remove alumina particles from the sample surface. Now the sample was ready for etching. The polishing machine used is shown in Fig. 3.10a.

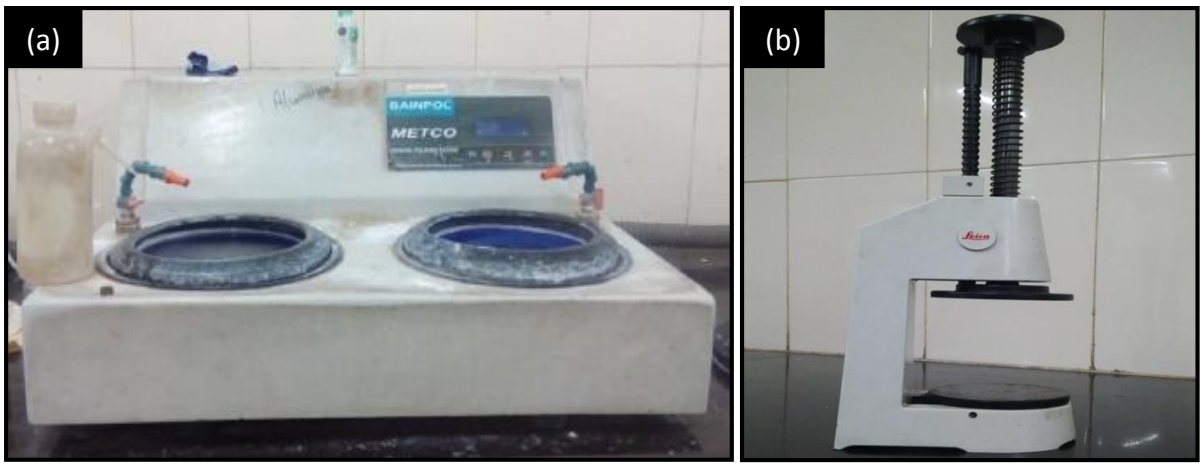

Figure 3.10: (a) Cloth polishing machine and (b) Levelling machine used in the present work.

(c) Etching

Etching is done to reveal different phases present in the metal/alloy system through selective chemical attack. Before polishing, the sample should be cleaned and dried properly. Different etchants are preferred for different type of steels. For dual phase steels, nital (2 % nitric acid in ethanol) is generally used to reveal the microstructure. Under SEM, ferrite is etched as black and martensite as white. Under, optical microscopy, ferrite appears white and martensite appears black, if etched with natal. The etchant should be prepared carefully and the etching time should be optimized for a specific steel to avoid over-etching.

(d) Levelling machine

To see the microstructure under optical microscope, the sample should be levelled and flat, otherwise the image would be out of focus. For this, levelling press shown in Fig. 3.11b was used, which pressed the sample into clay on the microscope slide, to get the flat and leveled

surface to be examined under optical microscope. A small piece of paper is used to cover the surface of specimen to avoid scratches while pressing.

3.4.5 Equipment used for microstructural evaluation

Mechanical properties of steel depend on the volume fraction, distribution and morphology of different phases present in the microstructure. So, microstructural evaluation is important to correlate the obtained mechanical properties with the microstructure. In the present work, optical microscopy and scanning electron microscopy were used to evaluate the microstructure and deformation mechanisms present in the microstructure.

(a) Optical microscope

The optical microscope (Make: Leica DM2500 M; *Lieca Microsystems*, Wetzlar, Germany) was used in the present study and is shown in Fig. 3.11. Optical microscope utilizes visible light and a system of lenses to magnify the area of the sample surface to be examined. This magnified image can be seen through eyepieces or in the integrated computer and can be stored in hard drive in any of the available formats for further use. The sample can be seen at different magnifications available on the optical microscope.

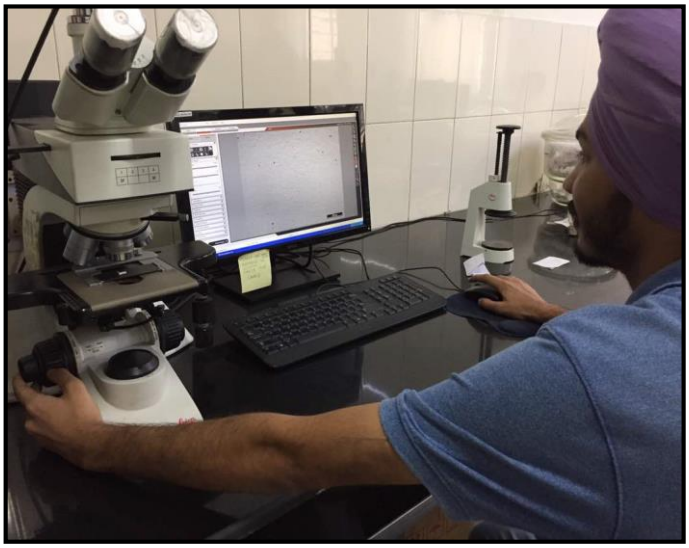

Figure 3.11: Optical microscope used in the present work.

(b) Field Emission Scanning Electron Microscope (FE-SEM)

FE-SEM set-up (FEI Nova Nano SEM 430, Field Emission Inc., Hillsboro, USA) was used to study the fracture surfaces of specimens after tensile testing at different strain rates. Samples were cut from the necked region to study the mechanisms of micro-cracks during deformation. The width of scanning area in FE-SEM varied from 1 cm–5 μm and maginification varied from 20 X–1,00,000 X.

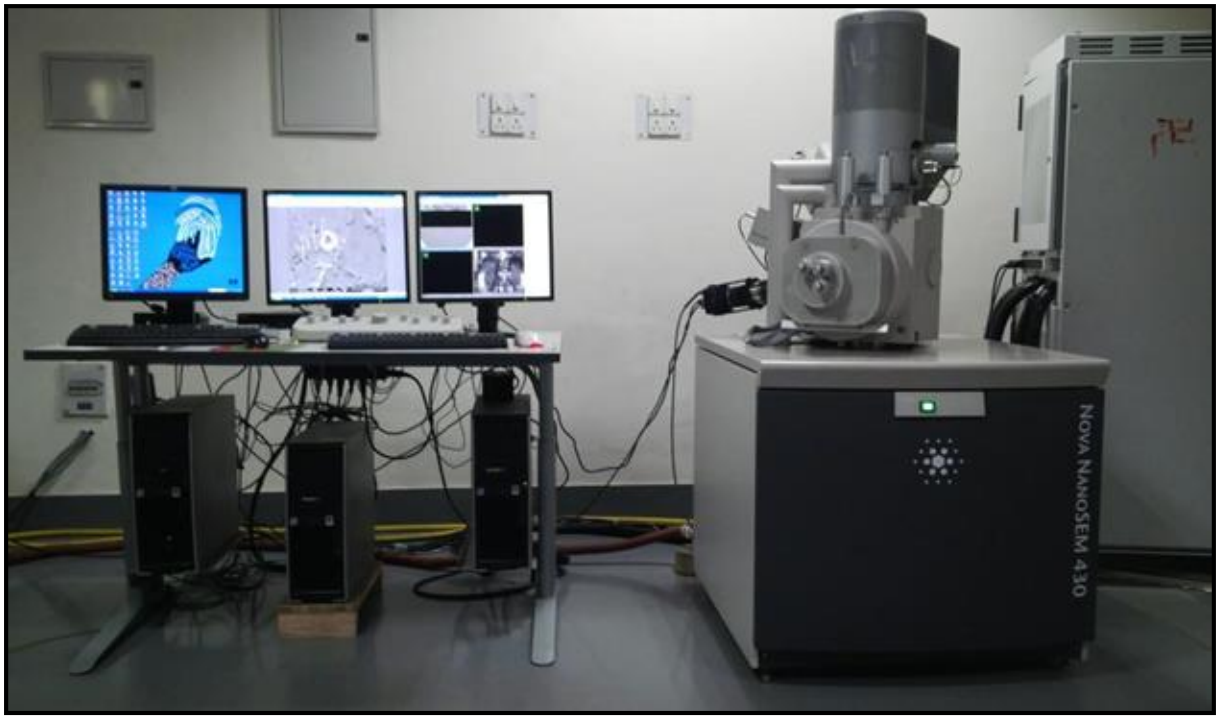

Figure 3.12: FE-SEM set-up used for microstructural characterization in the present work.

3.5 Summary of the chapter

In this chapter, the objective of the present research work and the key issues to be taken up during the work were discussed. The experimental procedure followed during research work and the procedure to prepare high strain rate samples were discussed in detail. Furthermore, the equipment used for annealing of samples, tensile testing at quasi-static and high strain rates, sample preparation and microstructure evaluation were discussed.

Chapter 4
Results and Discussion

4 Results and Discussion

4.1 General

This chapter provides details of various results of the present research work in a sequential manner. The tensile test data obtained by testing at different strain rates is presented in this chapter and the different properties like strain hardening behavior, strain rate sensitivity, uniform elongation, and ultimate tensile strength are obtained from this tensile data. SEM micrographs of the as-processed samples, and fractographs of the fracture tips of deformed samples after testing at different strain rates are shown in this chapter. The obtained properties after tensile testing are correlated with the micro-mechanisms of deformation. Furthermore the possible reasons behind the obtained results are also discussed in this chapter.

4.2 Microstructures obtained through various annealing cycles

SEM micrographs of steel specimens obtained after processing the as-received steel by three different annealing routes are shown in Fig. 4.1 (black regions represent ferrite and white regions represent martensite phase). The DP microstructure obtained by CAL route consisted of ferrite matrix with martensite phase distributed mostly on the grain boundaries of ferrite i.e. microstructure comprised of ferrite and grain boundary martensite (see Fig. 4.1a). For the microstructure obtained by CHCL route, martensite formation tendency was more within the ferrite grains or 'in-grain' ferrite sites (Fig. 4.1b). It consisted mainly of ferrite matrix with martensite phase distributed both at grain boundaries (grain boundary martensite) as well as within ferrite grains (in-grain martensite). Both CAL and CHCL contained about 20 % of volume fraction of martensite (MVF ~ 20 %) present in their respective microstructures. Finally, the microstructure obtained by CAS process consisted of core and shell type DP microstructure (as reported in the work of Kumar *et al*. [63]) in which martensite grains were surrounded by ferrite network/channel (Fig. 4.1c). The CAS steel possessed 67 % of martensite (MVF ~ 67 %) in the microstructure. Therefore, a shift from ferrite dominant microstructure to a martensite dominant microstructure was obtained.

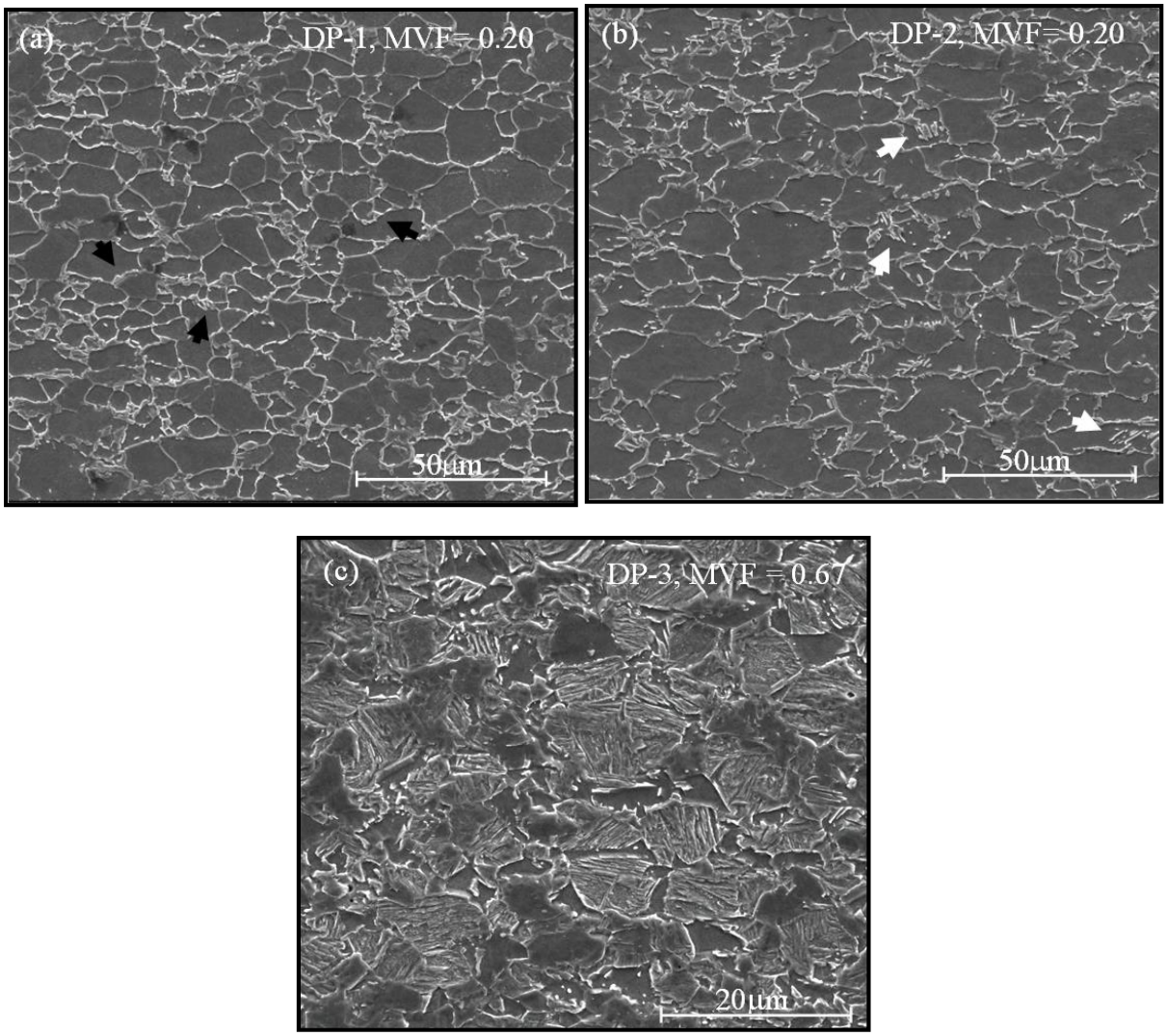

Figure 4.1: SEM Micrographs obtained after processing of as-received steel through (a) CAL, (b) CHCL, and (c) CAS. Black arrows indicate grain boundary martensite and white arrows indicate in-grain martensite.

4.3 Tensile properties under quasi-static strain rate conditions

Figure 4.2 shows the comparison of tensile deformation behaviour under quasi-static conditions of the three different dual phase microstructures. The evaluated tensile properties are also shown in Table 4.1. CAL and CHCL processing routes showed similar yield strength (YS), but the ultimate tensile stress (UTS) of CHCL was slightly higher than CAL with comparable ductility. The CHCL processed DP steel contained more in-grain martensite along with grain boundary martensite for same MVF (as compared to CAL processed DP steel). This change in microstructure increased the strength, with almost similar percentage elongation. The presence of in-grain martensite distribution in CHCL led to increase in strain hardening due to the higher restriction to dislocation motion by in-grain martensite. Consequently, strength of CHCL (DP-2 steel) was higher than CAL processed steel (DP-1 steel). Further, remarkable increase in strength was observed for the CAS processed steel due

to increased volume fraction of martensite (MVF ~ 67 %). The core and shell type microstructure provided much higher initial strain hardening of DP steel.

Table 4.1: Tensile properties of different DP steels under quasi-static conditions.

Annealing route	Resulting microstructure	Yield strength (MPa)	Ultimate tensile strength (MPa)	Percentage elongation (%)
CAL	DP-1	270	586	26.8
CHCL	DP-2	279	628	23.9
CAS	DP-3	800	1125	5.50

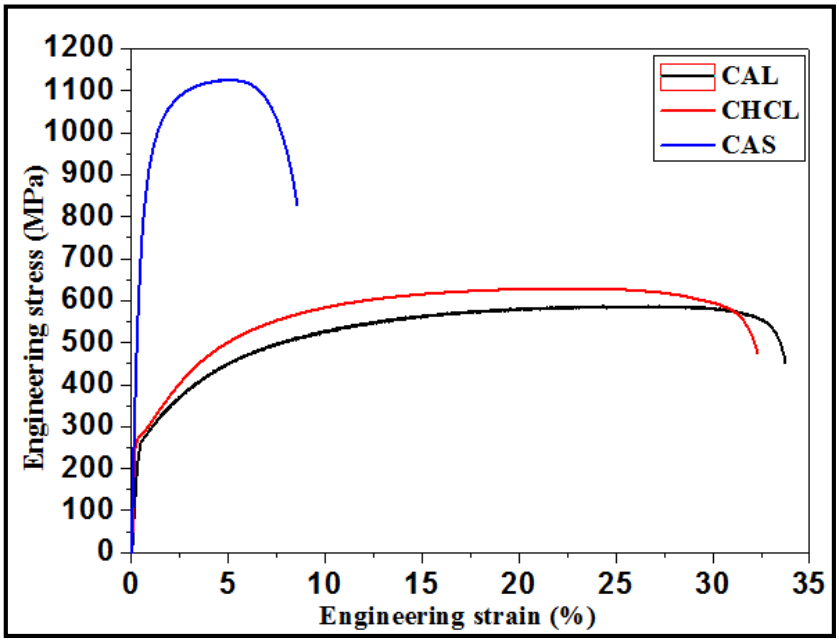

Figure 4.2: Engineering stress-strain plots of different DP steels under quasi-static conditions (2.7×10^{-4} s^{-1}).

4.4 Tensile properties under high strain rate conditions

The engineering stress-strain plots under quasi-static condition (2.7×10^{-4} s^{-1}) and various high strain rate conditions (100, 200, 500, and 650 s^{-1}) for the three DP steels are shown in Fig. 4.3a–c. For all the three steels (DP-1, DP-2, and DP-3), YS as well as UTS were observed to generally increase with increase in strain rate. However, the trend of change in uniform elongation with strain rate was not same across the three steels. For CAL and CHCL processed steels (i.e. DP-1 and DP-2 steels), there was decrease in uniform elongation with increase in strain rate. However, for the CAS processed steel (DP-3 steel), the trend was opposite i.e. there was increase in uniform elongation with increase in strain rate. The variation in UTS and uniform elongation with strain rate for the three DP steels is shown in Fig. 4.4.

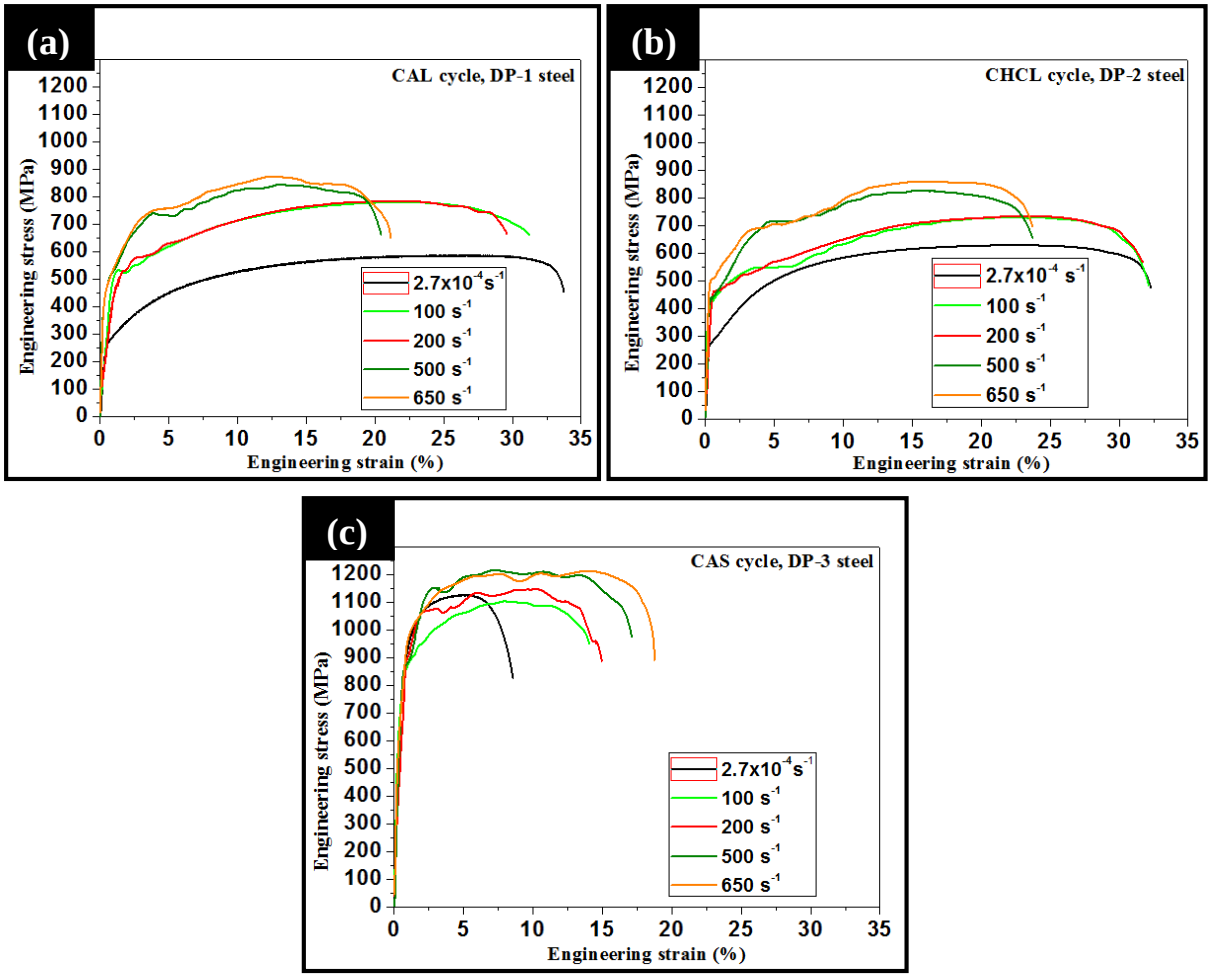

Figure 4.3: Engineering stress-strain curves under various strain rates for (a) DP-1, (b) DP-2, and (c) DP-3 steels.

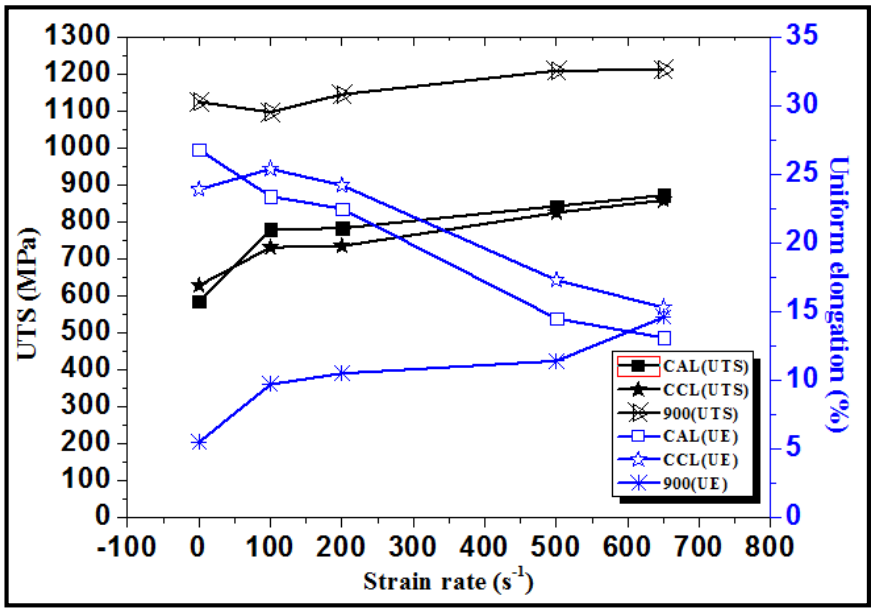

Figure 4.4: Change in UTS and uniform elongation, of various DP steels with change in strain rate from 2.7×10^{-4} to 650 s^{-1}.

For DP steels having less martensite fraction and large amount of ferrite phase (e.g. the conventional DP590 steel), work hardening is a predominant phenomenon, both at quasi-

static as well as high strain rates. This is due to the high strain rate hardening and work hardening capability of ferrite phase [1, 28, 41]. Further, with increase in strain rate, work hardening increases because of increase in dislocation density, thereby resulting in higher strengths at higher strain rates [60]. DP-1 and DP-2 steels contained ferrite as the primary phase (ferrite volume fraction ~ 80 %; MVF~20 %, in both DP-1 and DP-2 steels), and therefore in these steels, YS and UTS increased with increase in strain rate. For the same reasons, percentage elongation of DP-1 and DP-2 steels continuously decreased with increase in strain rate (see Fig. 4.3a–b, and Fig. 4.4). However, for DP steels having large amount of martensite phase (e.g. DP 1000 steel), there are two contradictory effects viz. work hardening and work softening, which come into action with change in strain rate. Under high strain rate testing conditions, adiabatic heating of specimen occurs resulting in softening of martensite phase present in steel, with the effect that strength of steel decreases and percentage elongation increases [28, 41, 79]. This effect is called work softening. Under quasi-static strain rate conditions, work hardening factor generally dominates and tends to increase the strength with increase in strain rate. However, at higher strain rates, the work softening factor tends to dominate [28, 41, 79]. Unlike DP-1 and DP-2 steels, the DP-3 steel contained martensite as the primary phase (MVF~67 %). In case of DP-3 steel, for increase in strain rate from quasi-static condition to high strain rate of 100 s^{-1}, work softening factor (softening of martensite due to adiabatic heating) resulted in greater decrease in strength compared to the increase in strength because of work hardening factor. The net effect was slight decrease in strength at strain rate of 100 s^{-1} compared to quasi-static conditions. However, with further increase in strain rate ($>$ 100 s^{-1}), the strength increased continuously showing dominance of work hardening over work softening factor. These results are consistent with the reported findings in literature [1, 41, 52, 79]. Further, DP-3 steel showed continuous increase in percentage elongation with increase in strain rate. This increase was attributed to the combined effect work softening and presence of core-shell type of microstructure (as reported by Kumar *et al.* [63]).

These observations were further corroborated with the help of FE-SEM micrographs of the three DP microstructures near fracture surface at high strain rate conditions. Figure 4.5 presents the micrographs for various steels for one typical high strain rate condition of 500 s^{-1}. For the entire high strain rate regime, DP-2 steel showed better percentage elongation than DP-1 steel.

It was observed that presence of in-grain martensite distribution in DP-2 steels restricted the growth of micro-cracks initiated at the ferrite-martensite interface regions. The micro-cracks initiated in DP-1 samples showed large growth (see Fig. 4.5a) whereas those in DP-2 samples were observed to get blunt because of the surrounding ferrite phase (see Fig. 4.5b). This phenomenon delayed the onset of global deformation and hence increased the ductility of DP-2 samples compared to DP-1 samples.

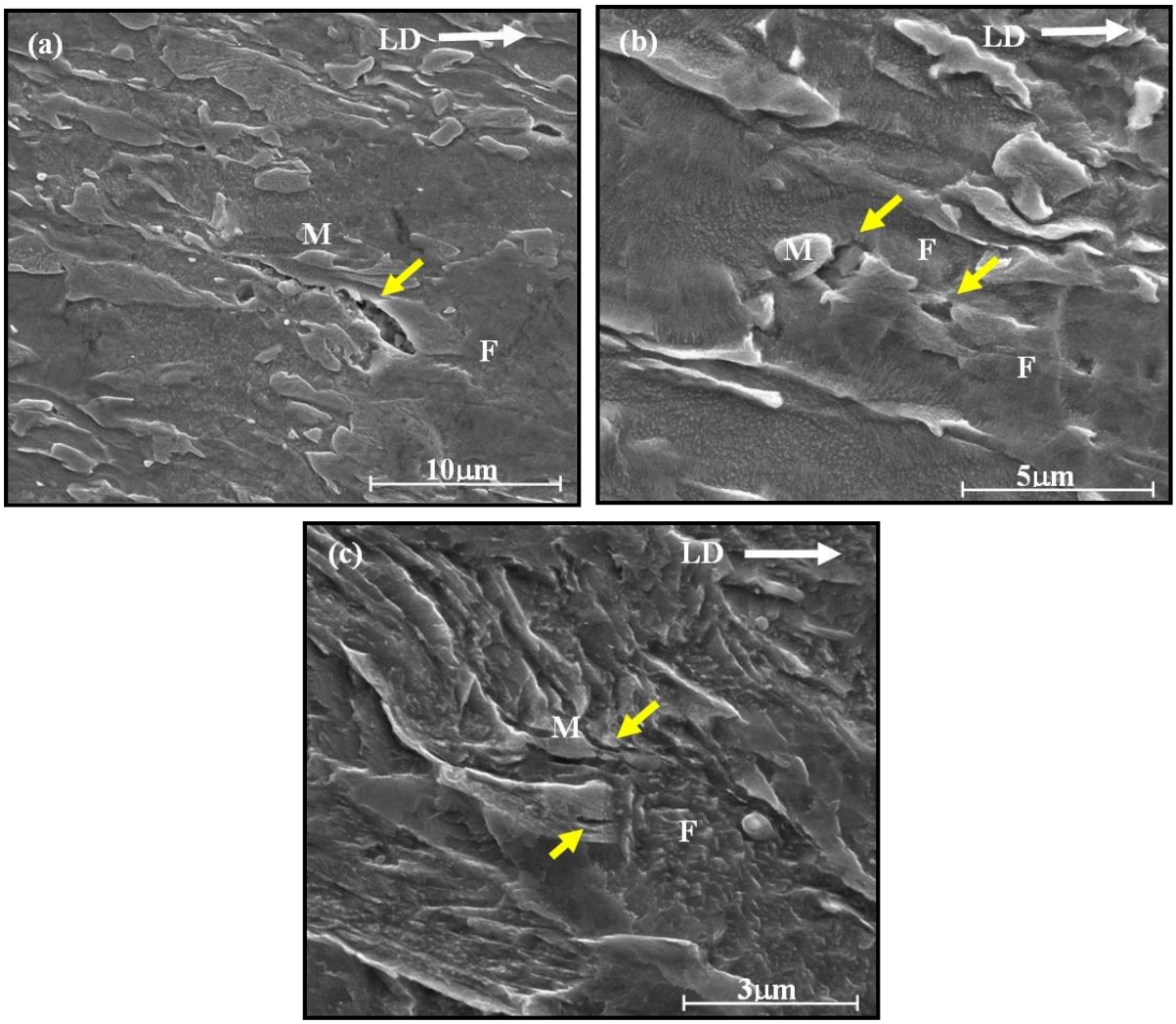

Figure 4.5: FE-SEM micrographs showing micro-cracks at ferrite-martensite interface near fracture tip of specimens tested at strain rate of 500 s^{-1} presenting (a) large growth of micro-crack in DP-1 sample, (b–c) showing blunting of cracks in ferrite in DP-2 and DP-3 samples respectively. White arrows indicate tensile loading direction and yellow arrows indicate micro-cracks. F and M indicate ferrite and martensite respectively.

Also, the increase in percentage elongation of DP-3 samples at high strain rates was supported by the FE-SEM micrograph shown in Fig. 4.5c. The micrograph showed highly deformed martensite and also blunting of micro-cracks by the surrounding ferrite phase. The micro-cracks initiated in the inter-lath martensite and got blunt in the surrounding ferrite. As a result the growth of micro-cracks was restricted by presence of ferrite channel around the

martensite grains, thereby enhancing the ductility. The percentage elongation of DP-3 steel increased from 5.5 % under quasi-static condition to 11.4 % at 500 s^{-1} to 14.5 % at 650 s^{-1}. Thus, DP-3 steel showed excellent strength-ductility combination at high strain rate conditions. These excellent results in DP-3 steels were attributed to the combined effect of adiabatic softening of martensite (due to high strain rate testing) and presence of core-shell type microstructure (due to CAS processing route).

Further, the strain rate sensitivity values were calculated for DP-1, DP-2, and DP-3 steels for the dynamic region (100–650 s^{-1}) for various true strain values. Figure 4.6 presents the results of strain rate sensitivity analysis for various steels for one typical true strain level of 5 % (ϵ = 0.05). DP-1 and DP-2 steels showed positive strain rate sensitivity throughout the entire strain rate range (from quasi-static to 650 s^{-1}) whereas DP-3 steel showed positive sensitivity throughout the dynamic range but negative sensitivity for quasi-static to 100 s^{-1} (beginning of dynamic region; also observed in Fig. 4.3c and Fig. 4.4).

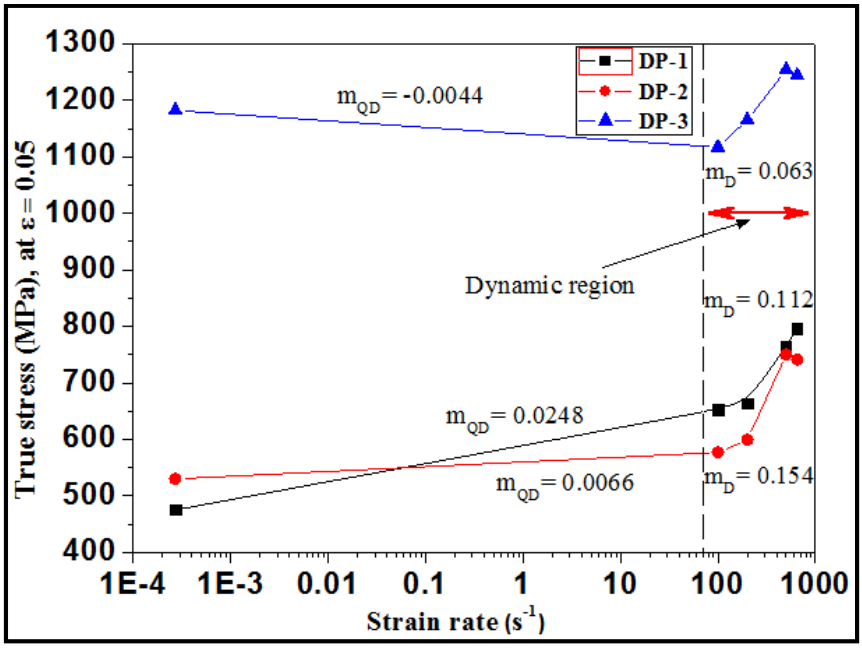

Figure 4.6: Results of strain rate sensitivity analysis for various DP steels at 5% true strain level. m_{QD} indicates strain rate sensitivity values when shifting from quasi-static to dynamic region and m_D indicates strain rate sensitivity values in the high strain rate dynamic region.

Also, it can be observed from Fig. 4.6 that all steels showed higher strain rate sensitivity in the dynamic strain rate region (m-value range: 0.063–0.1544) compared to when shifting from quasi-static to dynamic region i.e. quasi-static condition to 100 s^{-1} (m-value range: 0.0044–0.0248). Strain rate sensitivity is largely influenced by the solid solution hardened phases, like ferrite. Among the three steels studied, the CAS process, produced microstructure containing predominantly martensite than the rest. Martensite has the least

affinity towards strain rate hardening because of its asymmetric crystal structure. Because of the asymmetry, less glide planes for the dislocations are present in martensite. As a result, the martensite crystals fail to accommodate dislocations with increase in strain rate. This is the reason for which the stress increment for CAS processed steel when strain rate increased was very small.

4.5 Strain hardening behavior under various strain rate conditions

The variation in strain hardening rate with increase in true strain under quasi-static conditions is presented in Fig. 4.7 for the three different DP microstructures. Further, the ln(dσ/dε) versus ln(σ) plots obtained by the modified Crussard-Jaoul method are shown in Fig. 4.8. The three distinct stages of strain hardening characteristic are clearly observed from the plot (Fig. 4.8). Further, the values of strain hardening exponent (m) for different stages, and the true strain (ε) values at transition from one stage to the other are also presented in Fig. 4.8.

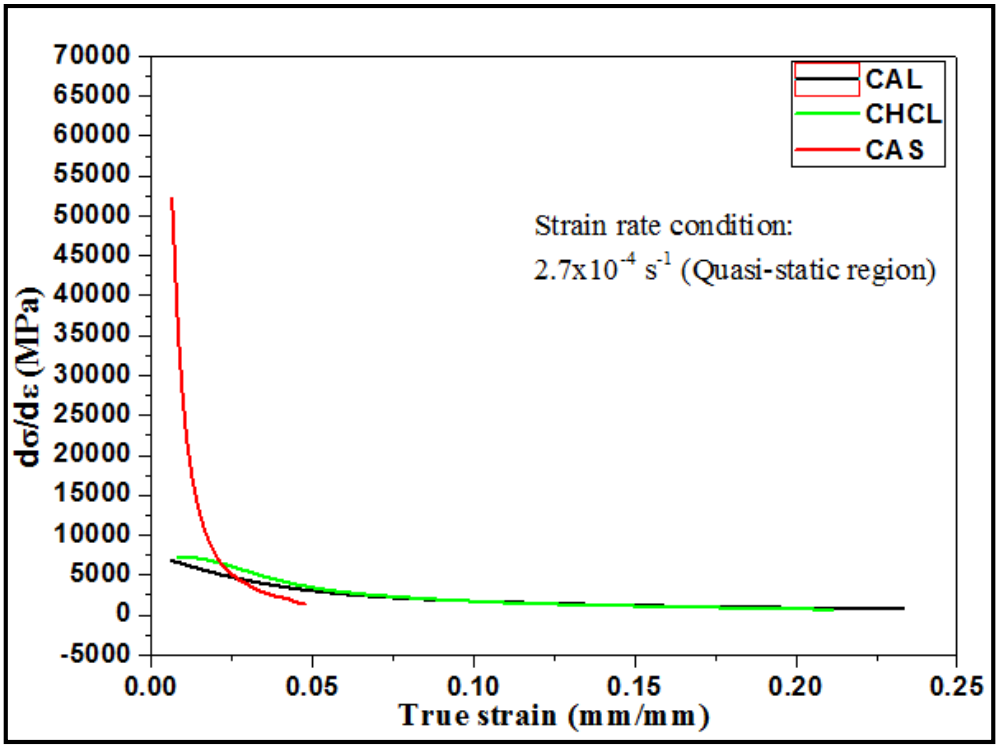

Figure 4.7: Variations in strain hardening rate with true strain under quasi-static conditions for the three different DP steels.

It can be observed from Fig. 4.3 that the initial strain hardening rate of CAS processed steel (DP-3 microstructure) was the highest, followed by CHCL route (DP-2 microstructure), and finally CAL route (DP-1 microstructure) with the lowest value. The highest initial strain hardening rate shown by DP-3 steel was attributed to the higher martensite fraction (MVF = 67 %) in DP-3 microstructure [74, 75, 78].

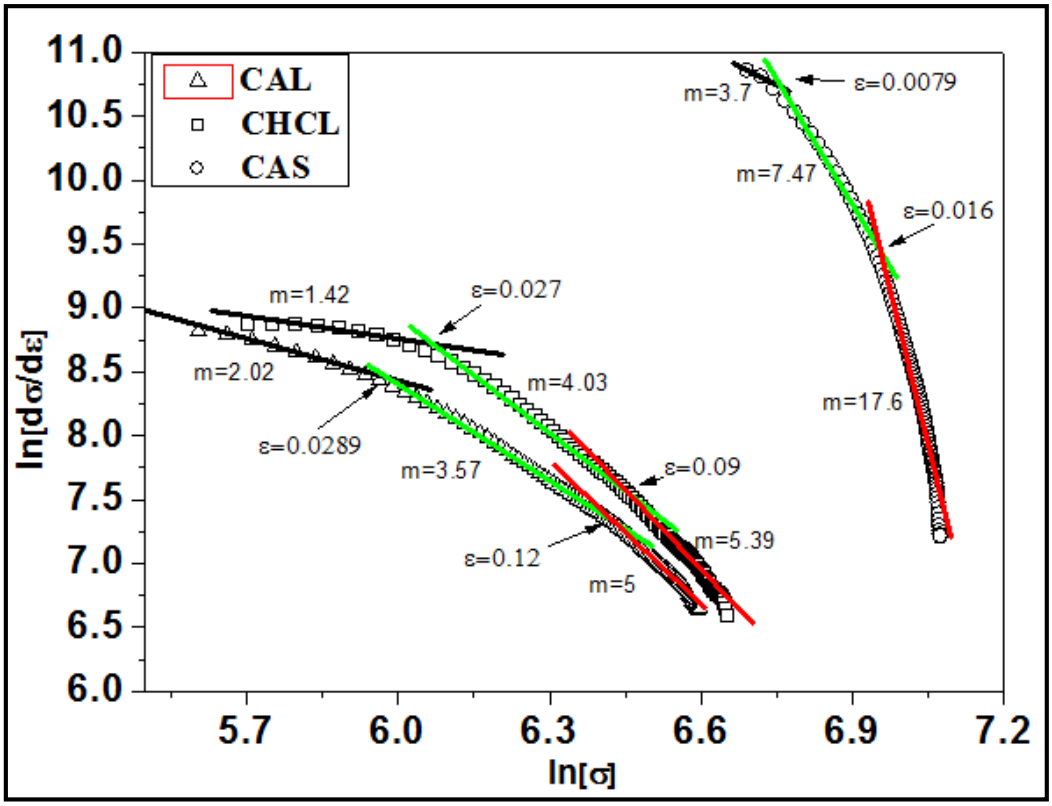

Figure 4.8: ln(dσ/dε) versus ln(σ) plots for the three DP steels based on modified C-J method. Strain hardening exponent (m) for different stages and true strain values (ε) at the transition of deformation stages are also shown.

Further, presence of in-grain martensite phase in DP-2 steel (for the same martensite fraction as in DP-1) provided more resistance to movement of dislocations as compared to DP-1 structure, resulting in higher initial strain hardening rate of DP-2 steel (as compared to DP-1). Figures 4.7–4.8 showed that the strain hardening rate of DP-2 was higher than DP-1, and the curves of CAL and CHCL cycles converged at 0.088 true strain (see Fig. 4.7). This strain value ($\in$ = 0.088) covered the entire range of second stage deformation of DP-2 steel (see Fig. 4.8). Thus, it was attributed that the higher strain hardening of DP-2 steel up to 0.088 true strain was due to the higher restrictions to deformation of ferrite phase provided by the in-grain martensite in DP-2 steel. The strain hardening rate curves of CAL and CAS converged at 0.027 true strain (see Fig. 4.7). This strain value ($\in$ = 0.027) covered more than half the portion of third stage deformation of DP-3 steel (see Fig. 4.8). Here, it may be noted that third stage of strain hardening is mainly dependent on deformation of martensite phase. For the DP-3 steel, martensite fraction was more (MVF = 67 %) as compared to DP-1/DP-2 steels (MVF = 20 %) with the result that martensite phase present in DP-3 steel contained lesser carbon and hence was softer than martensite of DP-1/DP-2 steels. The softer martensite present in DP-3 steel resulted in higher strain hardening rate.

The variation in strain hardening rate with increase in true strain for the three different DP microstructures under high strain rate conditions is presented in Fig. 4.9.

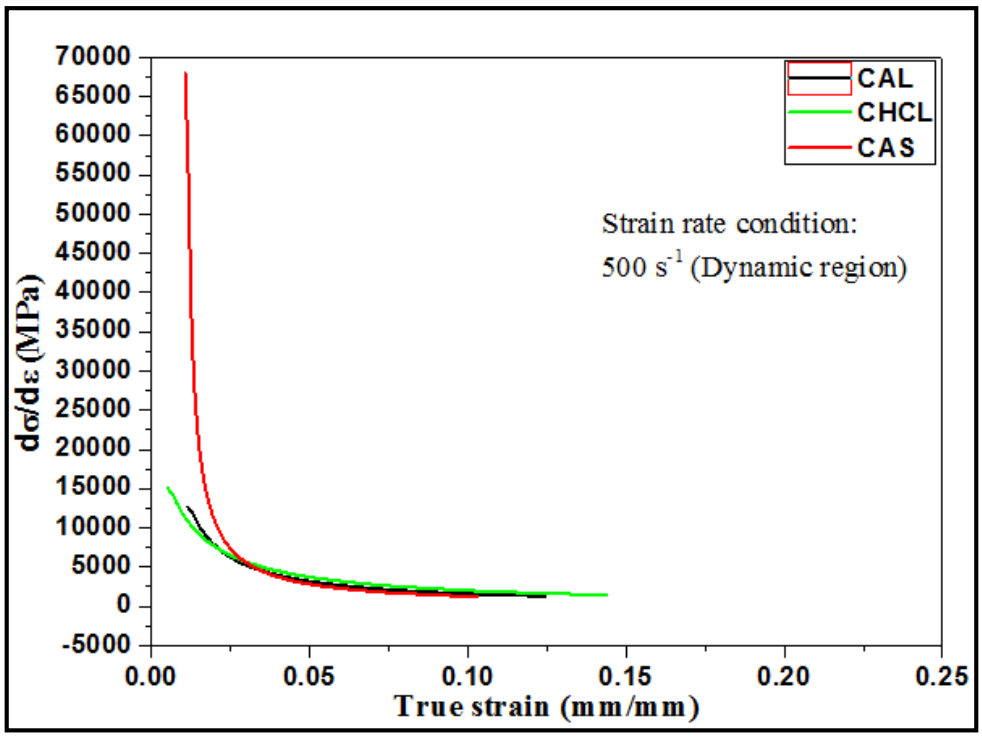

Figure 4.9: Variations in strain hardening rate with true strain under high strain rate of 500 s^{-1} for the three different DP steels.

It was observed that change in strain rate from quasi-static to dynamic region has significant impact on the initial stages of strain hardening rate (i.e. for low values of true strain). It was observed by comparing Fig. 4.7 and Fig. 4.9 that at high strain rate values, higher initial strain hardening rate was obtained as compared to quasi-static condition, for all DP steels. The plastic deformation in dual phase steels is largely controlled by the dislocation generation in the ferrite phase. The martensite phase acts as a barrier and it creates sufficient obstacles for the dislocations for further propagation. As a result, the dislocation pile up in the ferrite creates significant back stress, for which high strain hardening rates are achieved. With increase in the strain rate, the matrix experiences massive dislocation generation and pile up, which further escalates the back stress. The strain hardening rates thus increase at higher strain rates [60].

4.6 Energy absorption capacity of various steels at different strain rates

The energy absorption intensity values (GPa%) for the three DP steels at different strain rates are shown in Fig. 4.10. For high strain rate conditions, CAS processed steel (DP-3) showed the highest energy absorption capability, followed by CHCL processed steel, and finally CAL processed steel with the lowest toughness value. As compared to DP-1 steel, the superior

ductility and comparable strength of DP-2 steel at high strain rates resulted in better energy absorption capability. Further, CAS processed steel showed 19.3 GPa% and 21.3 GPa% higher energy absorption intensity at strain rates of 500 and 650 s^{-1} respectively compared to the industrially used CAL processed steel. These significantly high toughness values obtained for CAS processed steel were attributed to the excellent strength-ductility combination obtained in this steel in the dynamic strain rate region.

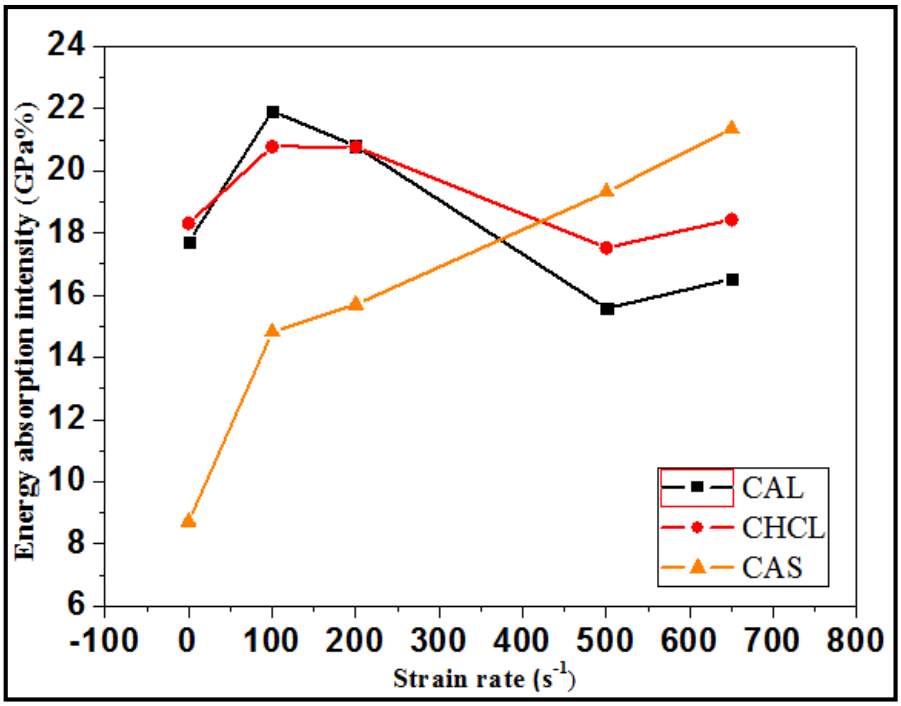

Figure 4.10: Energy absorption intensity values of the three DP steels at different strain rates.

4.7 Fracture analysis

The fracture surfaces of different DP steels under tensile testing at different strain rates were subjected to fractography studies under SEM. Typical fractographs are shown in Fig. 4.11a–c for high strain rate condition of 650 s^{-1}. DP-3 steel showed a distinct mixed mode fracture (containing features of both ductile as well as brittle fracture) under high strain rate conditions (see Fig. 4.11a). The fractograph of DP-3 steel showed cleavage fracture surrounded by dimples. The presence of large sized and deeper dimples in DP-3 steel at higher strain rates indicated higher ductility (as compared to under quasi-static conditions). Moreover at high strain rates, the adiabatic heating largely affects the constituent phases. In CAS steel, this effect was very much prominent. This further enhances the fact that, strain incompatibility between the ferrite and martensite was small in CAS steel [63]. Therefore, interface de-cohesion reduced at high strain rate in the CAS steel. At very high stress levels, the onset of martensite inter-lath interfaces crack occurred (see Fig. 4.5 and Fig. 4.12). The

growth or propagation of these micro cracks were restricted by surrounding ferrite (core-shell microstructure) and caused its blunting. This enhanced the ductility, hence energy absorption at high strain rates. This was due to the excellent strength-ductility combination in DP-3 steel at high strain rates. DP-1 and DP-2 steels showed ductile (dimple based) fracture predominantly, both at quasi-static and high strain rates. Figure 4.11b–c shows the fractographs of DP-1 and DP-2 steels respectively under high strain rate condition of 650 s^{-1}. It can be observed that under high strain rate conditions, the fractographs for both DP-1 and DP-2 steels show extensive amount of dimples which were shallow.

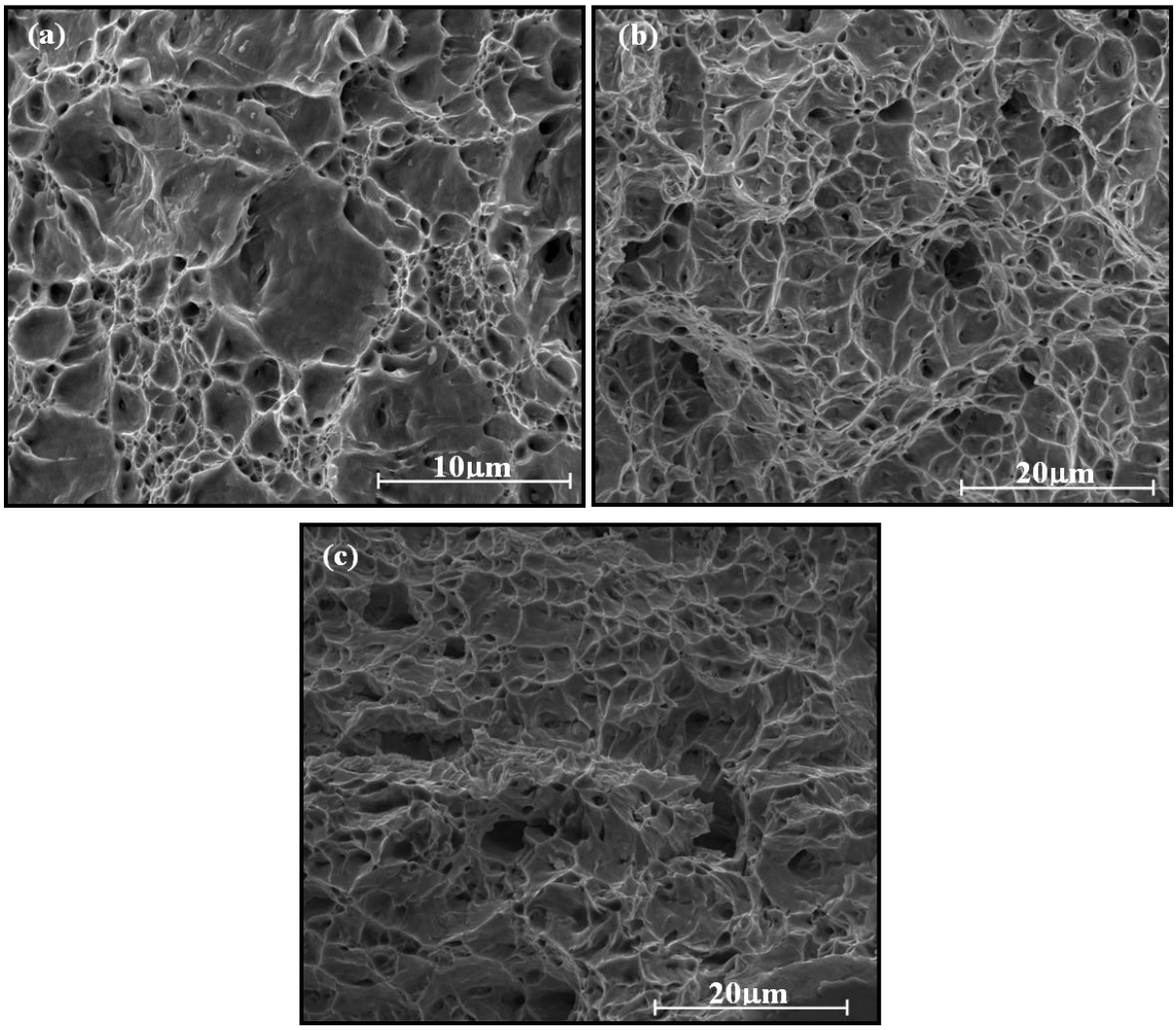

Figure 4.11: SEM fractographs of fracture surfaces of (a) DP-3 (b) DP-1, and (c) DP-2 steel at 650 s^{-1}.

The large number of dimples observed signify that both these steels failed due to ductile fracture (because of the large ferrite content in these steels) and shallow dimples signify loss in ductility (as compared to quasi-static conditions) and hence energy absorption capacity of these steels at high strain rates. To further confirm the results of fractography analysis, FE-SEM micrographs of the fracture tips of tensile specimens tested at a high strain rate of

500 s^{-1} were investigated as shown in Fig. 4.12. The ferrite-martensite interface de-cohesion was the prominent damage mechanism for the CAL processed steels at high strain rates. The void initiated at the interface propagated along the interface to create global damage (Fig. 4.5a). CHCL steel also exhibited interface de-cohesion as the main damage mechanism. But the voids formed in this case were not only imitated at the interface but also at the sites of in-grain martensite. Figure 4.5b shows the voids generated at the in-grain martensitic interface site, pointed by the yellow arrow. The micro-voids initiated at the in-grain martensite mostly form a spherical void rather than a macro-crack at the grain boundary interface (as seen for CAL).

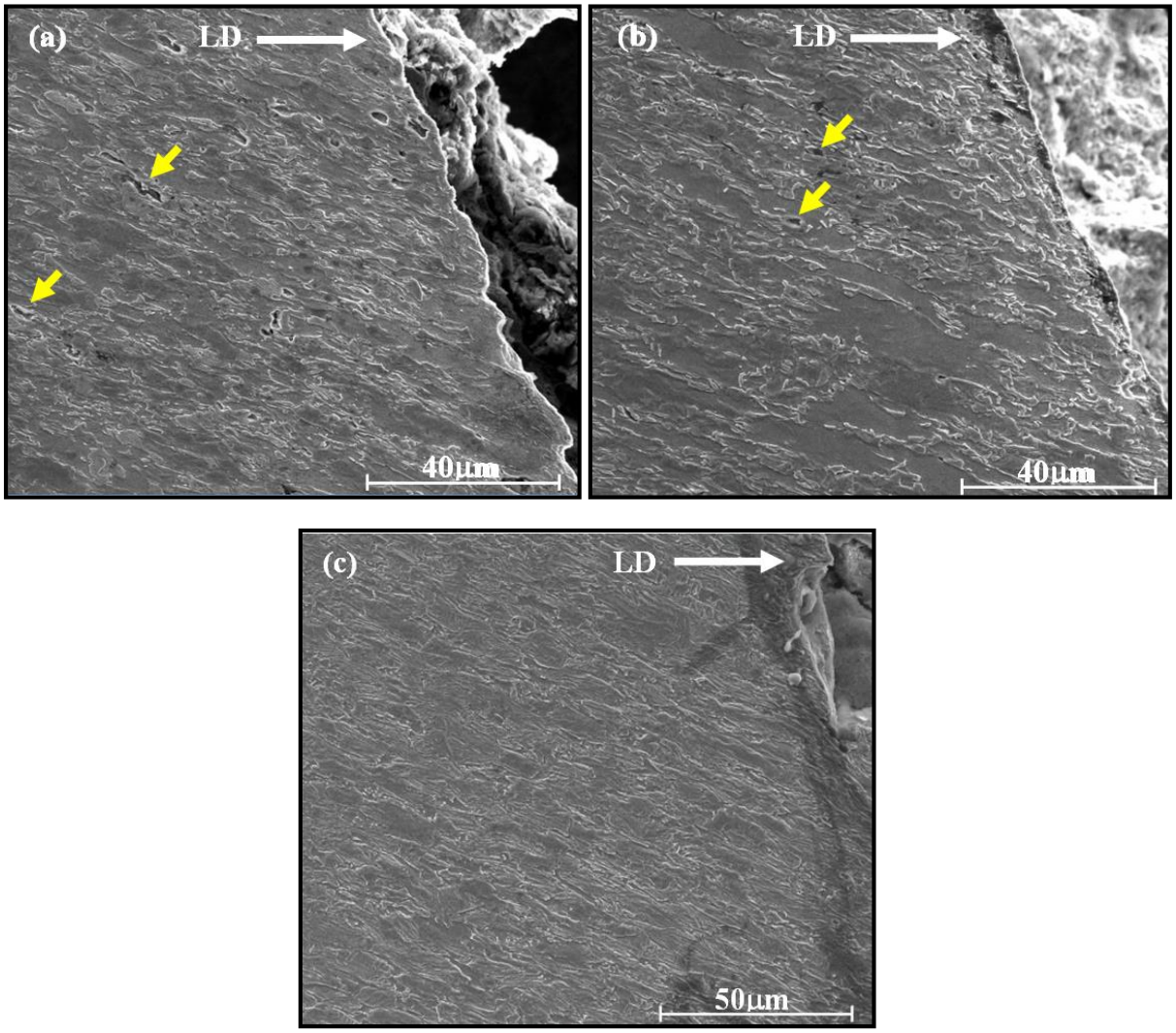

Figure 4.12: SEM micrographs of the fracture tip of tensile tested specimens of DP steels at strain rate of 500 s^{-1} for (a) DP-1 (b) DP-2, and (c) DP-3 steel. Yellow arrows indicate micro-cracks and white arrows show tensile loading direction.

These spherical voids at the in-grain interface grew uniformly and consumed higher energy before they coalesced. This delayed the fracture and thus a higher elongation was always

achieved for CHCL compared to CAL at high strain rates. Early fracture of the CAL in comparison to CHCL steel under quasi-static strain rate was reported by Chakraborty *et al.* (2016) [68]. For DP-1 and DP-2 steels, the microstructure near fracture tip showed presence of micro-cracks (see Fig. 4.12a–b). Further, the martensite islands present in these steels were interconnected as shown earlier in Fig. 4.1a–b. So, for DP-1 and DP-2 steels, once the crack initiated in martensite, it led to early failure due to inter-connectivity and brittle nature of the relatively high carbon martensite. However, for the DP-3 steel, the micro-cracks were not observed (see Fig. 4.12c) or appeared at a relatively later stage as compared to DP-1 and DP-2 steels. Further, the inter-connectivity of martensite islands in DP-3 steel was broken by the presence ferrite channels (see Fig. 4.1c). So, in case of DP-3 steel, even if micro-crack appeared in martensite, it may stop or retard the micro-crack due the shell type of ferrite around the martensite core (previously reported by Kumar *et al.* [63]). The stress triaxiality imposed by the surrounding martensite network to the ferrite grains in both, DP-1 and DP-2 steels decreased the ability of ferrite to absorb energy during deformation, while in case of DP-3 steel, there was no such hindrance for the deformation of ferrite, thus providing increased energy absorption intensity.

Chapter 5
Conclusions

5 Conclusions

5.1 General

This chapter includes the key findings and major conclusions of the present research work.

5.2 Annealing simulations

Three different annealing cycles viz. CAL, CHCL, and CAS cycle, were used to obtain three different DP microstructures having difference in volume fraction, distribution, and morphology of second phase martensite. The results obtained after processing of as-received steel by these three different processing routes are as following:

- The microstructure obtained by CAL (conventionally used in the industry) route consisted of ferrite matrix with martensite phase distributed on the grain boundaries of ferrite. The microstructure obtained by CHCL route consisted of ferrite matrix with martensite phase distributed both at grain boundaries (grain boundary martensite) as well as within ferrite grains (in-grain martensite. The microstructure obtained by CAS cycle consisted of core and shell type DP microstructure in which martensite grains were surrounded by ferrite network/channel.
- The quantitative analysis of microstructures (obtained by CAL and CHCL cycle) using Image J software showed that both the microstructures contained nearly same amount of martensite phase (MVF~20 %). The volume fraction of martensite was 67 % for the microstructure obtained by CAS cycle.
- The martensite islands were inter-connected and brittle (because of high carbon) in case of CAL and CHCL processed steels. The inter-connectivity of martensite islands was broken by the ferrite channel network in case of CAS processed steel.

5.3 Tensile testing at different strain rates

The three DP steels with different microstructures were further deformed at different strain rates of 2.7×10^{-4}, 100, 200, 500, and 650 s^{-1}. The tensile data obtained from these tests was used to plot stress-strain plots and to evaluate the different properties of three steels like strain hardening, strain rate sensitivity and energy absorption capacity. The important findings obtained from the comparison of the properties of three different steels were as following:

- Under quasi-static conditions, CAS processed samples (DP-3) showed the highest UTS, followed by CHCL (DP-2) and then CAL processed samples (DP-1). The order of percentage elongation was CHCL (DP-2), followed by CAL (DP-1), and finally CAS (DP-3) processed samples with the lowest ductility. The presence of in-grain martensite in DP-2 samples and typical core-shell microstructure with high martensite fraction in DP-3 samples resulted in these properties.
- All the three DP steels showed increase in strength values (both YS and UTS) with increase in strain rates. In case of CAL and CHCL samples, uniform elongation decreased with increase in strain rate, but for CAS processed steel elongation increased remarkably at higher strain rate. The changes in properties were observed due to changes in the two main phenomena of work hardening and work softening.
- All the three steels showed three stages of strain hardening at quasi-static strain rate. For all strain rate levels, the initial strain hardening rate of CAS processed steel (DP-3 microstructure) was the highest, followed by CHCL route (DP-2 microstructure), and finally CAL route (DP-1 microstructure) with the lowest value. The strain hardening rates of all the dual phase steels increased with strain rate. The increase was significant in the initial strain levels, but, at higher strains, it saturated with no significant difference between different strain rates.
- All steels showed higher strain rate sensitivity in the dynamic strain rate region (m-value range: 0.063–0.1544) compared to when shifting from quasi-static to dynamic region i.e. quasi-static condition to 100 s^{-1} (m-value range: 0.0044–0.0248).
- For high strain rate conditions, CAS processed steel (DP-3) showed the highest energy absorption capability, followed by CHCL processed steel, and finally CAL processed steel with the lowest toughness values.

5.4 Microstructure characterization of deformed samples

Microstructures of the deformed specimens at different strain rates were observed near the fracture end. Also the fracture surfaces of the three DP steels were subjected to fractographic analysis under SEM. The important results obtained were as follows:

- In case of CAL samples, cracks initiated because of ferrite-martensite interface de-cohesion at the ferrite grain boundaries. However, in case of CHCL samples, the cracks initiated at the in-grain martensite interface along with grain boundary interfaces. In case of CAS processed steel, cracks initiated from the inter-lath interface.

- It was observed that presence of in-grain martensite distribution in DP-2 steels restricted the growth of micro-cracks initiated at the ferrite-martensite interface regions. The micro-cracks initiated in DP-1 samples showed large growth whereas those in DP-2 samples got blunt because of the surrounding ferrite phase. This phenomenon delayed the onset of global deformation and hence increased the ductility of DP-2 samples compared to DP-1 samples. In case of DP-3 steel, the growth of micro-cracks initiated from the inter-lath interface was restricted by presence of ferrite channel around the martensite grains. Also adiabatic heating led to softening of martensite phase. These two factors enhanced the ductility of DP-3 steel under high strain rate conditions.
- CAL and CHCL samples showed ductile (dimple based) fracture predominantly, both at quasi-static and high strain rate conditions. CAS processed steel showed a distinct mixed mode fracture (containing features of both ductile as well as brittle fracture) under all strain rate conditions. The presence of large sized and deeper dimples in CAS samples at higher strain rates indicated higher ductility.

5.5 Major conclusions

The present study shows the scope of microstructure engineering to produce high strength dual phase steels needed for crashworthy design of automobiles. The present research shows that the morphology and spatial distribution of second phase martensite is crucial in attaining a good combination of high strength and ductility. The influence of change in strain rate on the deformation behavior was also analyzed. The main conclusions are as follows:

- The martensite morphology, distribution and volume fraction significantly influence the properties of DP steels, both under quasi-static and high strain rate conditions. Under quasi-static conditions, CHCL processed steel (DP-2) shows maximum energy absorption capacity but for dynamic strain rate conditions, CAS processed steel (DP-3) provides best toughness/crash worthiness.
- The core and shell type microstructure and high martensite fraction in CAS processed steel is very effective in increasing the ductility at high strain rates. Ferrite surrounding martensite in CAS steel, restricts the growth of cracks emanating from the inter-lath interface of martensite grains. Moreover, adiabatic heating at high strain rates softens the martensite phase and increases its plasticity. This reduces the strain incompatibility between the existing phases, thus resulting in better percentage elongation.

5.6 Future scope

The present research work studied the influence of martensite volume fraction, distribution and morphology on the properties of DP steels at different strain rates in the range of 2.7×10^{-4}–650 s^{-1} under room temperature. However the following points can be taken care off for future studies in this area.

- Further investigations can be done by varying the temperature during tensile testing at different strain rates.
- Due to the shortage of time and availability of equipment, intermediate strain rates between 2.7×10^{-4}–100 s^{-1} and high strain rates in excess of 650 s^{-1} have not been covered in the present work. Thus it can be further investigated.
- Furthermore, the bulge test, hole expansion ratio studies, and or parameters viz. Lankford parameter, planar anisotropy etc. can be investigated for various steels to check their formability.
- Further research can be done to improve the core/shell like microstructure. The volume fraction of ferrite and martensite phases (in core and shell type microstructure) can be optimized to further improve the mechanical properties under high strain rate conditions.

References

1. A. Uenishi, H. Yoshida, S. Yonemura, S. Hiwatashi, S. Hirose, N. Suzuki, High strain rate properties of high strength steel sheets, International Journal of Automobile Engineering 2 (2011) 109–113.
2. E. Cadoni, N.K. Singh, M.K. Singh, N.K. Gupta, Strain rate behaviour of multi-phase and complex-phase steels for automotive applications, In: 10th International Conference on the Mechanical and Physical Behaviour of Materials under Dynamic Loading, Freiburg, Germany, 2nd-7th September, 2012, EPJ Web of Conferences 26, 05003 (2012).
3. J. Slycken, P. Verleysen, J. Degrieck, J. Bouquerel, Characterisation of the high strain rate properties of Advanced High Strength Steels, High Performance Structures and Materials III 85 (2006) 259–268.
4. T. Nanda, V. Singh, V. Singh, A. Chakraborty, S. Sharma, Third generation of advanced high-strength steels: Processing routes and properties, Journal of Materials: Design and Applications DOI: 10.1177/1464420716664198.
5. R. Kuziak, R. Kawalla, S. Waengler, Advanced high strength steels for automotive industry, Archives of Civil and Mechanical Engineering 8 (2008) 103–117.
6. M. Mukherjee, T. Bhattacharyya, S.B. Singh, Models for austenite to martensite transformation in TRIP-aided steels: a comparative study, Materials and Manufacturing Processes 25(1–3) (2010) 206–210.
7. P. Simon, P.D. Beggs, A numerical performance comparison of a dual-phase steel and aluminium alloy bumper bar system, International Journal of Crashworthiness 15 (2010) 425–442.
8. Q.U. Hao, Advanced high strength steel through para equilibrium carbon partitioning and austenite stabilization. Ph. D. Dissertation, Case Western Reserve University, USA, 2011.
9. O.N. Cora, M. Koc, Promises and problems of ultra/advanced high strength steel (U/AHSS) utilization in automotive industry. In: The 7th Otomotiv Teknolojileri Kongresi (ed Solmaz E, Kaya N, Öztürk F), Bursa, Turkey, 26 May–27 May 2014, Uludag University, Bursa, 2014.
10. D.K. Matlock, J.G. Speer, Processing opportunities for new advanced high-strength sheet steels, Materials and Manufacturing Processes 25(1) (2010) 7–13.
11. D.K. Matlock, J.G. Speer, E.D. Moor, P.J. Gibbs, Recent developments in advanced high strength sheet steels for automotive applications: An overview, Journal of Engineering Science & Technology 15(1) (2012) 1–12.

12. S. Maggi, M. Murgia, Introduction to the metallurgic characteristics of advanced high strength steels for automobile applications, Welding International 22 (2008) 610–618.
13. G. Weber, H. Thommes, H. Gaul, O. Hahn, M. Rethmeier, Mechanical properties of weld bonded joints of advanced high strength steels, Journal of Adhesion Science and Technology 25 (2011) 2369–2389.
14. O. Kwon, K. Lee, G. Kim, K.G. Chin, New trends in advanced high strength steel developments for automotive applications, Materials Science Forum 638–642 (2010) 136–141.
15. M. Kassar, W. Yu, Design of automotive structural components using high strength sheet steels: the effect of strain rate on mechanical properties of sheet steels, A Research Project Sponsored by the American Iron and Steel Institute, University of Missouri-Rolla Rolla, Missouri, 1989.
16. T. Rahmaan, A. Bardelcik, J. Imbert, C. Butcher, M.J. Worswick, Effect of strain rate on flow stress and anisotropy of DP600, TRIP780, and AA5182-O sheet metal alloys, International Journal of Impact Engineering 88 (2016) 72–90.
17. H. Huh, J. H. Lim, S. H. Park, High speed tensile test of steel sheets for the stress-strain curve at the intermediate strain rate, International Journal of Automotive Technology 10(2) (2009) 195−204.
18. S. Li, Y. Kang, G. Zhu, S. Kuang, Effects of strain rates on mechanical properties and fracture mechanism of DP780 dual phase steel, Journal of Materials Engineering and Performance 24 (2015) 2426–2434.
19. F.M. Al-Abbasi, Predicting the effect of ultrafine ferrite on the deformation behaviour of DP-steels, Computational Materials Science 119 (2016) 90–107.
20. R.R. Mohanty, O.A. Girina, N.M. Fonstein, Effect of heating rate on the austenite formation in low-carbon high-strength steels annealed in the inter-critical region, Metallurgical and Materials Transaction A 42 (2011) 3680–3690.
21. N. Saeidi, A. Ekrami, Comparison of mechanical properties of martensite/ferrite and bainite/ferrite dual phase 4340 steels, Materials Science & Engineering A 523 (2009) 125–129.
22. R.A. Mohammad, A. Ekrami, Effect of ferrite volume fraction on work hardening behaviour of high bainite dual phase (DP) steels, Materials Science & Engineering A 477 (2008) 306–310.
23. D.K. Mondal, R.K. Ray, Microstructural changes and kinetics of recrystallization in a few dual-phase steels, Steel Research International 60(1) (1989) 33–40.

24. A.K. Lis, B. Gajda, Modelling of the DP and TRIP microstructure in the C–Mn–Al–Si automotive steel, Journal of Achievements in Materials and Manufacturing Engineering 15(1–2) (2006) 127–134.
25. L.P. Karjalainen, M.C. Somani, Physical simulation studies on the kinetics of the recrystallization and austenite decomposition in steels. In: Proceedings of international conference on thermomechanical simulation and processing of steels (SimPro'04), R&D Centre for Iron & Steel, SAIL, Ranchi, India, 2004.
26. D. Farias, Influence of microstructure on the corrosion performance of DP steels. Ph.D. Dissertation, Eindhoven University of Technology, Colombia (2014).
27. D. Matlock, J. Speer, Constitutive behavior of high strength multiphase sheet steels under high strain rate deformation conditions. Project by Advanced Steel Processing and Products, Research Centre, Department of Metallurgical and Materials Engineering, Colorado School of Mines, Golden, Colorado (2005).
28. N.D. Beynon, T.B. Jones, G. Fourlaris, Effect of high strain rate deformation on microstructure of strip steels tested under dynamic tensile conditions, Materials Science and Technology 21 (2005) 103–112.
29. C. A. Thompson, High strain rate characterization of advanced high strength steels. M.S Dissertation, University of Waterloo, Ontario, Canada (2006).
30. J. Adamczyk, A. Grajcar, Effect of heat treatment conditions on the structure and mechanical properties of DP-type steel, Journal of Achievements in Materials and Manufacturing Engineering 17 (2006) 305–308.
31. M.K. Manoj, V. Pancholi, S.K. Nath, Mechanical properties and fracture behaviour of medium carbon dual phase steels, International Journal of Research in Advent Technology 2(4) (2014) 243–249.
32. S. Sodjit, V. Uthaisangsuk, Microstructure based prediction of strain hardening behavior of dual phase steels, Materials and Design 41 (2012) 370–379.
33. L. Gao, Y.M. Zhou, J.L. Liu, X.D. Shen, Z.M. Ren, Effect of water quenching process on the microstructure and magnetic property of cold rolled dual phase steel, Journal of Magnetism and Magnetic Materials 322(8) (2010) 929–933.
34. Q. Meng, J. Li, J. Wang, Z. Zhang, L. Zhang, Effect of water quenching process on microstructure and tensile properties of low alloy cold rolled dual-phase steel, Materials and Design 30 (2009) 2379–2385.

35. L.V.D.L. Concepción, N.H. Lorusso, G.H. Svobod, Effect of carbon content on microstructure and mechanical properties of dual phase steels, Procedia Materials Science 8 (2015) 1047–1056.
36. Z. Li, T.S. Wang, X.J. Zhang, F.C. Zhang, Annealing softening behaviour of cold-rolled low-carbon steel with a dual-phase structure and the resulting tensile properties, Materials Science and Engineering A 552 (2012) 204–210.
37. K.N. Singh, E. Cadoni, K.M. Singh, K.N. Gupta, Mechanical behavior of Advanced High Strength Steel at high strain rates, Applied Mechanics and Materials 82 (2011) 178–183.
38. M. Sarwar, E. Ahmad, K.A. Qureshi, T. Manzoor, Influence of epitaxial ferrite on tensile properties of dual phase steel, Materials and Design 28 (2007) 335–340.
39. D.K. Mondal, R.M. Dey, Effect of grain size on the microstructure and mechanical properties of a C-Mn-V dual-phase steel, Materials Science and Engineering A 149 (1992) 173–181.
40. Y. Cao, J. Ahlström, B. Karlsson, The influence of temperatures and strain rates on the mechanical behaviour of dual phase steel in different conditions, Journal of Materials Research and Technology 4(1) (2015) 68–74.
41. W. Wang, M. Li, C. He, X. Wei, D. Wang, H. Du, Experimental study on high strain rate behaviour of high strength 600–1000 MPa dual phase steels and 1200 MPa fully martensitic steels, Materials and Design 47 (2013) 510–521.
42. R.G. Davies, Influence of martensite composition and content on the properties of dual phase steels, Metallurgical and Materials Transaction: A 9 (1978) 671–679.
43. Y. Granbom, Structure and mechanical properties of dual phase steels – an experimental and theoretical analysis. Ph.D. Dissertation, Royal Institute of Technology, Sweden (2010).
44. X.J. He, N. Tera, A. Berghezan, Influence of martensite morphology and its dispersion on mechanical properties and fracture mechanisms of Fe-Mn-C dual-phase steels, Journal of Matal Science 18 (1984) 367–373.
45. S.K. Paul, M. Mukherjee, S. Kundu, S. Chandra, Prediction of hole expansion ratio for automotive grade steels, Computational Materials Science 89 (2014) 189–197.
46. J. Wang, G. Li, A. Xiao, Bainite-ferrite multi-phase steel strengthened by Ti-micro alloying, Materials Transactions 52 (2011) 2027–2031.
47. Q. Meng, J. Li, H. Zheng, High-efficiency fast-heating annealing of a cold-rolled dual-phase steel, Materials & Design 58 (2014) 194–197.

48. H. Mohrbacher, Modern steel grades and advanced steel semi-products for automotive body applications, Metal 24 (2005) 1–13.
49. H. Lorusso, A. Burgueno, D. Egidi, H. Svoboda, Application of dual phase steels in wires for reinforcement of concrete structures, Procedia Materials Science 1 (2012) 118–125.
50. S. Aktas, U. Ozsarac, S. Aslanlar, Effect of spot welding parameters on tensile properties of DP 600 steel sheet joints, Materials and Manufacturing Processes 27 (2012) 756–764.
51. W. Wang, X. Wei, The effect of martensite volume and distribution on shear fracture propagation of 600–1000 MPa dual phase sheet steels in the process of deep drawing, Internal Journal of Mechanical Sciences 67 (2013) 100–107.
52. Y. Cao, B. Karlsson, J. Ahlström, Temperature and strain rate effects on the mechanical behaviour of dual phase steel, Materials Science & Engineering A 636 (2015) 124–132.
53. J. H. Kim, D. Kim, H. N. Han, F. Barlat, M.G. Lee, Strain rate dependent tensile behavior of advanced high strength steels: Experiment and constitutive modelling, Materials Science & Engineering A 559 (2013) 222–231.
54. L.V.D.L. Concepción, N.H. Lorusso, G.H. Svobod, Effect of carbon content on microstructure and mechanical properties of dual phase steels, Procedia Materials Science 8 (2015) 1047–1056.
55. P.D. Sudersanan, N. Kori, S. Aprameyan, U.N. Kempaiah, The effect of carbon content in martensite on the strength of dual phase steel, International Journal of Industrial Engineering and Management Science 2 (2012) 1–4.
56. A. Uenishi, H. Yoshida, Y. Kuriyama, M. Takahashi, Material characterization at high strain rates for optimizing car body structures for crash events, Nippon Steel Technical Report No. 88 July 2003.
57. R. Gerlach, C. Kettenbeil, N. Petrinic, A new split Hopkinson tensile bar design, International Journal of Impact Engineering 50 (2012) 63–67.
58. E. Cadoni, N.K. Singh, D. Forni, M.K. Singh, N.K. Gupta, Strain rate effects on the mechanical behaviour of two dual phase steels in tension, The European Physical Journal Special Topics 225 (2016) 409–421.
59. V. Colla, M.D. Sanctis, A. Dimatteo, G. Lovicu, A. Solina, R. Valentini, Strain hardening behavior of dual-phase steels, Metallurgical and Materials Transactions A 40(A) (2009) 2557–2567.
60. A. Das, M. Ghosh, S. Tarafder, S. Sivaprasad, D. Chakrabarti, Micro mechanisms of deformation in dual phase steels at high strain rates, Material Science & Engineering A 680 (2017) 249–258.

61. S. Kim, S. Lee, Effects of martensite morphology and volume fraction on quasi-static and dynamic deformation behavior of dual-phase steels, Metallurgical and Materials Transactions A 31(A) (2000) 1753−1760.
62. H. Huh, S.B. Kim, J.H. Song, J.H. Lim, Dynamic tensile characteristics of TRIP-type and DP-type steel sheets for an auto-body, International Journal of Mechanical Sciences 50 (2008) 918–931.
63. B.R. Kumar, N.K. Patel, K. Mukherjee, M. Walunj, G.K. Mandal, T. Venugopalan, Ferrite channel effect on ductility and strain hardenability of ultra high strength dual phase steel, Materials Science & Engineering A 685 (2017) 187–193.
64. Q. Hao, S. Qin, Y. Liu, X. Zuo, N. Chen, W. Huang, Y. Rong, Effect of retained austenite on the dynamic tensile behavior of novel quenching-partitioning-tempering martensitic steel, Materials Science & Engineering A 662 (2016) 16–25.
65. M. Erdogan, S. Tekeli, The effect of martensite volume fraction and particle size on the tensile properties of a surface-carburized AISI 8620 steel with a dual-phase core microstructure, Materials Characterization 49(5) (2002) 445–454.
66. J. Zhang, H. Di, Y. Deng, R.D.K. Misra, Effect of martensite morphology and volume fraction on strain hardening and fracture behavior of martensite-ferrite dual phase steel, Materials Science and Engineering A 627 (2015) 230–240.
67. V. Singh, M. Adhikary, T. Venugopalan, A. Chakraborty, T. Nanda, B. R. Kumar, Role of recrystallization and pearlite dissolution in industrial processing of DP590 steels, Materials and Manufacturing Processes DOI: 10.1080/10426914.2017.1317792.
68. A. Chakraborty, M. Adhikary, T.Venugopalan, V. Singh, T. Nanda, B.R. Kumar, Effect of ferrite-martensite interface morphology on bake hardening response of DP590 steel, Materials Science & Engineering A 676 (2016) 463–473.
69. A.G. Kalashami, A. Kermanpur, E. Ghassemali, A. Najafizadeh, Y. Mazaheri. Correlation of microstructure and strain hardening behavior in the ultrafine-grained Nb-bearing dual phase steels, Materials Science & Engineering A 678 (2016) 215–226.
70. G.C. Soares, B.M. Gonzalez, L.D.A. Santos, Strain hardening behavior and microstructural evolution during plastic deformation of dual phase, non-grain oriented electrical and AISI 304 steels, Materials Science & Engineering A 684 (2017) 577–585.
71. Y. Tomita, K. Okabayashi, Tensile stress-strain analysis of cold worked metals and steels and dual-phase steels, Metallurgical and Materials Transactions A 16(A) (1985) 865–872.

72. J. Zhang, H. Di, Y. Deng, R.D.K. Misra, Effect of martensite morphology and volume fraction on strain hardening and fracture behaviour of martensite–ferrite dual phase steel, Materials Science & Engineering A 627 (2015) 230–240.
73. C.N. Li, F.Q. Ji , G.Yuan, J. Kang, R.D.K. Misra, G.D. Wang, The impact of thermo-mechanical controlled processing on structure-property relationship and strain hardening behavior in dual-phase steels, Materials Science & Engineering A 662 (2016) 100–110.
74. Y. Bergstrom, Y. Granbom, D. Sterkenburg, A dislocation-based theory for the deformation hardening behavior of dp steels: impact of martensite content and ferrite grain size, Journal of Metallurgy Doi.org/10.1155/2010/647198.
75. H. Ashrafi, M. Shamanian, R. Emadi, N. Saeidi, Correlation of tensile properties and strain hardening behavior with martensite volume fraction in dual-phase steels, Transactions-Indian Institute of Metals 70(6) (2017) 1575–1584.
76. J. Luo, M.Q. Li, Strain rate sensitivity and strain hardening exponent during the isothermal compression of Ti60 alloy, Materials Science and Engineering A 538 (2012) 156–163.
77. Q. Li, X. Huang, W. Huang, Microstructure and mechanical properties of a medium-carbon bainitic steel by a novel quenching and dynamic partitioning (Q-DP) process, Materials Science & Engineering A 662 (2016) 129–135.
78. Z.P. Xiong, A.G. Kostryzhev, N.E. Stanford, E.V. Pereloma, Microstructures and mechanical properties of dual phase steel produced by laboratory simulated strip casting, Materials and Design 88 (2015) 537–549.
79. Y. Gao, C. Xu, Z.P. He, Y.L. He, L.Li, Response characteristics and adiabatic heating during high strain rate for TRIP steel and DP steel, Journal of Iron and Steel Research, International 22(1) (2015) 48–54.